Radiocarbon in the land and ocean component of the Community Earth System Model

Tobias Frischknecht[1], Altug Ekici[1], and Fortunat Joos[1]

[1]University of Bern

November 21, 2022

Abstract

Large amounts of the carbon-isotope ^{14}C, entering Earth's carbon cycle, were produced in the atmosphere by atomic bomb tests in the 1950s and 1960s. Here, we forced the ocean and land components of the Community Earth System Model with atmospheric $^{14}CO_2$ over the historical period to constrain overturning time scales and fluxes. The uptake of bomb ^{14}C by the land model is lower than observation-based estimates. This mismatch is likely linked to too low ^{14}C uptake by vegetation as the model overestimates ^{14}C/C ratios of modern soils indicating model biases in forest productivity or wood carbon allocation and turnover. The ocean model matches the observation-based global bomb ^{14}C inventories when applying the Large and Yeager wind data and the quadratic relationship between gas transfer piston velocity and wind speed of Wanninkhof, 2014. However, ocean bomb ^{14}C inventories are underestimated in simulations with winds from the Japanese Reanalysis Project, calling for an upward revision of the piston velocity by 15% for this wind product. The sum of ocean, land, and atmospheric bomb ^{14}C inventory changes is lower in the 1960s than reconstructed bomb ^{14}C production, likely due to uncertainties in the observational production and atmospheric records and too low land model ^{14}C uptake. Simulated natural radiocarbon ages in the deep ocean are many centuries older than data-based estimates, indicating too slow deep ocean ventilation. Our study suggests that ^{14}C observations are key to constrain carbon fluxes and transport timescales within Earth system models.

1 **Radiocarbon in the land and ocean component of the Community Earth**

2 **System Model**

3 **Tobias Frischknecht[1], Altug Ekici[1], Fortunat Joos[1]**

4 [1]Climate and Environmental Physics, Physics Institute and Oeschger Centre for Climate Change

5 Research, University of Bern, Switzerland

6 Corresponding author: Fortunat Joos (joos@climate.unibe.ch)

7

8 **Key Points:**   (< 140 characters)

9 The uptake of bomb-produced ^{14}C by the ocean and land is simulated with the Parallel Ocean

10 Model POP2 and the Community Land Model CLM5

11 ^{14}C uptake by CLM5 is lower than observational estimates and carbon allocation and overturning

12 in forest ecosystems are biased.

13 The deep ocean of POP2 is ventilated too slowly and radiocarbon ages are several centuries older

14 than estimates from observations

15

16 **Abstract (< 250 words)** 242 words

17 Large amounts of the carbon-isotope ^{14}C, entering Earth's carbon cycle, were produced in the

18 atmosphere by atomic bomb tests in the 1950s and 1960s. Here, we forced the ocean and land

19 components of the Community Earth System Model with atmospheric $^{14}CO_2$ over the historical

20 period to constrain overturning time scales and fluxes. The uptake of bomb ^{14}C by the land model

21 is lower than observation-based estimates. This mismatch is likely linked to too low ^{14}C uptake

22 by vegetation as the model overestimates ^{14}C/C ratios of modern soils indicating model biases in

23 forest productivity or wood carbon allocation and turnover. The ocean model matches the

24 observation-based global bomb ^{14}C inventories when applying the Large and Yeager wind data

25 and the quadratic relationship between gas transfer piston velocity and wind speed of

26 Wanninkhof, 2014. However, ocean bomb ^{14}C inventories are underestimated in simulations with

27 winds from the Japanese Reanalysis Project, calling for an upward revision of the piston velocity

28 by 15% for this wind product. The sum of ocean, land, and atmospheric bomb ^{14}C inventory

29 changes is lower in the 1960s than reconstructed bomb ^{14}C production, likely due to uncertainties

30 in the observational production and atmospheric records and too low land model ^{14}C uptake.

31 Simulated natural radiocarbon ages in the deep ocean are many centuries older than data-based

32 estimates, indicating too slow deep ocean ventilation. Our study suggests that ^{14}C observations

33 are key to constrain carbon fluxes and transport timescales within Earth system models.

34

35 **Index Terms:** 0414 Biogeochemical cycles, processes, and modeling; 0428 Carbon cycling;

36 1622 Earth system modeling; 1635 Oceans; 4504 Air/sea interactions

37 **Keywords:** Radiocarbon, bomb ^{14}C, land biosphere, gas transfer piston velocity, deep ocean

38 ventilation.

39

40 **1. Introduction**

41

42 Radiocarbon (^{14}C) is produced naturally in the upper atmosphere by cosmic rays (Masarik and

43 Beer, 2009). In addition, large amounts of ^{14}C were injected into the stratosphere as a byproduct

44 of nuclear bomb tests in the 1950s and 1960s (Enting, 1982). Natural and bomb-produced ^{14}C is

45 quickly oxidized to $^{14}CO_2$ and becomes part of the Earth's carbon cycle (Siegenthaler, 1989).

46 ^{14}C, unlike the stable ^{12}C and ^{13}C isotopes, decays radioactively with a mean lifetime of 8200

47 years (Bé et al., 2013). The decay rate serves as a clock once carbon is isolated from the

48 atmosphere. Radioactive decay is too slow to have noticeably affected bomb ^{14}C up to now.

49 However, carbon in the deep ocean and soils is depleted in natural ^{14}C with respect to

50 atmospheric carbon because of radioactive decay (Revelle and Suess, 1957;Oeschger et al.,

51 1975). The slower the carbon exchange with the atmosphere the larger the depletion.

52 Observations of the transient, pulse-like bomb ^{14}C signal and the natural ^{14}C/C ratio provide

53 therefore constraints on the uncertain time scales of exchange of carbon and other tracers

54   between and within different Earth system components. These constraints are important as

55   correctly representing the overturning time scales (Bolin and Rodhe, 1973) and exchange fluxes

56   of carbon, heat, and other tracers is a prerequisite to reliably project the fate of anthropogenic

57   CO_2 and ultimately global warming.

58   The goal of this study is to evaluate the representation of key carbon fluxes and transport time

59   scales in the ocean and land components of the Community Earth System Model (CESM) with

60   ^{14}C observations. We rely on ^{14}C-enabled simulations over the historical and preindustrial

61   periods. Model results are compared to the observational evidence for the redistribution of bomb

62   ^{14}C among the atmosphere, ocean, and land biosphere, and the observation-based natural ^{14}C age

63   of the deep ocean. The Earth system budget of bomb ^{14}C is established by comparing bomb ^{14}C

64   production statistics and inventory changes in the atmosphere, ocean, and land biosphere.

65   The natural cycle of ^{14}C is strongly perturbed by human activities. Atmospheric $^{14}C/C$ varied

66   relatively little over the past few millennia before the first nuclear bombs detonated (Reimer et

67   al., 2020;Hogg et al., 2020). The tropospheric $^{14}C/C$ ratio almost doubled within a decade before

68   a nuclear test ban treaty was set in place in 1963 (Naegler and Levin, 2009a). Over time, this

69   bomb ^{14}C signal entered the ocean, vegetation, and soils (Lawrence et al., 2020;He et al.,

70   2016;Hesshaimer et al., 1994;Joos, 1994;Broecker et al., 1985) which caused a decline in the

71   tropospheric$^{14}C/C$ ratio and the ^{14}C inventory of the atmosphere after 1963. The emissions of

72   ^{14}C-free fossil CO_2 forced an additional negative trend in atmospheric $^{14}C/C$ (Graven,

73   2015;Naegler and Levin, 2006;Suess, 1955). Small anthropogenic ^{14}C sources stem from the

74   nuclear power industry (Zazzeri et al., 2018;Graven and Gruber, 2011). For convenience, the

75   terms "bomb" and "excess" are used interchangeably in this manuscript to describe the changes

76   in $^{14}C/C$ and ^{14}C inventories due to all processes, including natural variability, since 1945.

77   The ^{14}C variations of the recent past and the modern distribution of ^{14}C in the Earth system are

78   documented by compilations from various climate archives such as tree rings and corals

79   (Reimer, 2020;Dentith et al., 2019;Graven et al., 2012;Naegler and Levin, 2009a;Grottoli and

80   Eakin, 2007;Druffel, 2002), and modern sampling in the atmosphere, ocean, and land biosphere

81   (Turnbull et al., 2017;Levin et al., 2010;Key et al., 2004;He et al., 2016;Lawrence et al.,

82   2020;Shi et al., 2020). For comparison with observations and improved process understanding,

83   ^{14}C has been implemented in box models (Oeschger et al., 1975;Broecker et al.,

84   1985;Siegenthaler and Joos, 1992;Naegler and Levin, 2006), dynamic ocean circulation models

85   (Jahn et al., 2015;Mouchet, 2013;Toggweiler et al., 1989;Rodgers et al., 2004), spatially-

86   resolved land biosphere models (Koven et al., 2013;Roth and Joos, 2013;Randerson et al., 2002),

87   and atmospheric transport models (Rodgers et al., 2011;Krakauer et al., 2006;Randerson et al.,

88   2002;Braziunas et al., 1995). The ocean modeling community established protocols to simulate

89   the uptake and distribution of natural and bomb ^{14}C (Orr et al., 2017;Orr et al., 1999) for the

90   evaluation of transport time scales and water mass age (Khatiwala et al., 2012).

91   Measurements documenting bomb ^{14}C in vegetation and soils are relatively scarce and do not

92   permit to directly establish the bomb ^{14}C inventory of the global land biosphere. Naegler and

93   Levin (2009a) estimated the bomb ^{14}C evolution in the land biosphere by the difference between

94   total ^{14}C production estimated from bomb-test statistics, the observed change in the atmospheric

95   inventory and the observation-constrained uptake by the ocean. Naegler and Levin (2009b) used

96   their bomb inventory reconstruction in combination with a 3-box land biosphere model to

97   estimate global net primary productivity (NPP) to 41 to 64 GtC yr^{-1}. The representation of NPP

98   and carbon turnover time scales is essential to simulate the terrestrial sink of anthropogenic

99   carbon (Thompson et al., 1996). The global observational constraint of Naegler and Levin

100   (2009a) has, however, not yet been applied by others to evaluate NPP and carbon turnover of

101   spatially-resolved state-of-the-art terrestrial models.

102   Observations of the bomb ^{14}C tracer in the ocean are particularly useful to constrain the air-sea

103   gas transfer piston velocity (Broecker et al., 1985;Wanninkhof, 1992;Siegenthaler, 1989). The

104   piston velocity is a key parameter for the observational and modeling community and used to

105   compute air-sea fluxes of various gases as well as the marine carbon sink from observations of

106   the air-sea CO_2 partial pressure difference (Wanninkhof, 1992;Watson et al., 2020;Iida et al.,

107   2020). The piston velocity is typically parameterized as a function of wind speed (Woolf et al.,

108   2019). The scaling coefficients of these parameterizations have been determined with reduced

109   and intermediate complexity and transport matrix models by minimizing differences between the

110   observed and simulated bomb ^{14}C signal (Wanninkhof, 2014;Naegler, 2009;Müller et al.,

111   2008;Sweeney et al., 2007;Krakauer et al., 2006;Naegler et al., 2006) but uncertainties in the

112   piston velocity of order 20% remain (Wanninkhof, 2014; Naegler 2009). The values of the

113   scaling coefficients are closely tied to the applied wind product and need potentially to be

114   adjusted for different wind products. The application of different wind products in ^{14}C-enabled

115   ocean models, as in this study, offers the opportunity to evaluate the applied piston velocity

116   parameterization and its coefficients for specific wind products against observation-based global

117   ocean bomb ^{14}C inventory estimates.

118   The Earth system budget of bomb ^{14}C allows one to assess global exchange fluxes of carbon

119   between the atmosphere, ocean, and land biosphere and to test overall consistency of model

120   results and observations (Hesshaimer et al., 1994;Naegler and Levin, 2009a). Bomb ^{14}C

121   production records combined with observation-based estimates of the changes in the stratospheric

122   and tropospheric bomb ^{14}C inventories reveal the combined bomb ^{14}C uptake by the land and

123   ocean from the atmosphere.

124   While many studies are addressing ^{14}C in dynamic ocean models, ^{14}C simulations with spatially-

125   resolved land biosphere models are scarce and simulations with state-of-the-art Earth System

126   Models addressing the budget of bomb ^{14}C and air-sea and air-land fluxes are missing. Thus far,

127   the models participating in the Coupled Model Intercomparison Project (Eyring et al., 2016),

128   which are used for carbon cycle and climate projections in the assessments of the

129   Intergovernmental Panel on Climate Change, have generally not been evaluated against ^{14}C

130   observations.

131   Recently, carbon isotopes were added to the marine (Jahn et al., 2015) and land biosphere

132   components (Koven et al., 2013) of the Community Earth System Model (CESM). Shi et al.

133   (2020) compared Δ^{14}C of soil carbon as simulated with CLM5 with their soil Δ^{14}C data. Here, we

134   build on this earlier work and present results from ^{14}C-enabled simulations with the standard

135   version of POP2 with a nominal horizontal resolution of 1° and with the latest version 5 of CLM

136   for the preindustrial state and the historical period. POP2 and CLM5 are standard components of

137   CESM version 2. POP2 simulations over the historical period are performed with two wind

138   products, the Large and Yeager Normal Year Forcing (NYF, Large and Yeager (2009)) and the

139   Japanese Reanalysis project (JRA55, Kobayashi et al. (2015)) data, to investigate the sensitivity

140   of results to the wind forcing and the related piston velocity.

141   We analyze the bomb ^{14}C budgets of the Earth, the ocean, and the land biosphere to evaluate the

142   land and ocean components of CESM2. The modeled evolution of the bomb ^{14}C inventory of the

143   land biosphere is compared with the observational estimate of Naegler and Levin (2009a). We

144   further compare estimates of the global ocean bomb ^{14}C inventory established from marine

145   measurements, the temporal evolution of surface ocean $^{14}C/C$ during the bomb period as recorded

146   by corals and bivalves, and the gridded bomb $^{14}C/C$ data from the Global Ocean Data Analysis

147   Project (GLODAP) with model results. The observed changes in the atmospheric bomb ^{14}C

148   inventory and the bomb ^{14}C production record allow us to estimate whether the combined bomb

149   ^{14}C uptake by the ocean and the land biosphere models is simulated in agreement with

150   observations. Finally, we compare modeled and measured $^{14}C/C$ in the deep ocean to assess the

151   model's ventilation time scales.

152

153   **2. Methods**

154   **2.1 Isotopic Notation**

155   We adopt conventional isotopic notation. The $^{14}C/C$ ratio ($^{14}R_{sample}$) of a pool or sample is

156   reported as a deviation from a standard ratio ($^{14}R_{std}=1.176 \ 10^{-12}$) in permil (‰) using the so-called

157   Δ-notation. It holds $\Delta^{14}C_{sample}=(^{14}R_{sample,N} / ^{14}R_{std} -1)\cdot 1000$. Δ-values are corrected for

158   fractionation by normalizing $^{14}R_{sample}$ to a fixed $^{13}C/^{12}C$ ratio of -25 ‰. The normalized ratio is

159   $^{14}R_{sample,N}=^{14}R_{sample} (1-2 \ (\delta^{13}C_{sample}+25)/1000))$. $\delta^{13}C_{sample}$ is the deviation of the $^{13}C/^{12}C$ ratio of

160   the sample from a standard ratio ($^{13}R_{std}=0.0112372$) in permil and, similarly, $\delta^{14}C_{sample}$ is the

161   deviation of the $^{14}C/C$ ratio of the sample from $^{14}R_{std}$. It holds $\delta^i C=(^i R_{sample} / ^i R_{std} -1) \cdot 1000$ with

162   index i indicating the isotope. $\Delta^{14}C$ is then related to $\delta^{14}C$ and vice versa (Stuiver and Polach,

163   1977):

164   $$\Delta^{14}C = \delta^{14}C - 2(\delta^{13}C + 25)(1 + \frac{\delta^{14}C}{1000})$$ (1a)

165   $$\delta^{14}C = \frac{\Delta^{14}C + 2(\delta^{13}C+25)}{1 - \frac{2(\delta^{13}C+25)}{1000}}$$ (1b)

166   The isotopic fractionation α is related to the fractionation factor ε in permil units by

167   $\varepsilon =(\alpha-1)\cdot 1000$ (Mook, 1986).

168

169

2.2 Model description

171 The Community Earth System Model version 2 (CESM2) (Danabasoglu et al., 2020;Hurrell et
172 al., 2013) is a state-of-the-art Earth System Model developed by the National Centre for Climate
173 Research (NCAR), USA. Recently, the carbon isotopes ^{13}C and ^{14}C were added to the ocean
174 (Jahn et al., 2015) and land component (Keller et al., 2017;Koven et al., 2013;Oleson et al., 2013)
175 of CESM2. Jahn et al. applied a version of the Parallel Ocean Model version 2 (POP2) with a
176 horizontal resolution of about 3° to simulate the distribution of carbon, ^{13}C, and ^{14}C within the
177 ocean for the preindustrial state and the historical period. Koven et al. (2013) described the
178 implementation of a radiocarbon tracer within the Community Land Model version 4.5 (CLM4.5)
179 and compared modeled and observed ^{14}C soil profiles for a range of sites. In this study, we
180 applied the carbon isotope-enabled POP2 ocean (Danabasoglu et al., 2012;Danabasoglu et al.,
181 2020) and the most recent version 5.0 of CLM (Lombardozzi et al., 2020;Kennedy et al.,
182 2019;Lawrence et al., 2019). Both components are used in a so-called stand-alone mode and
183 driven by atmospheric forcing data (see section 2.3). A brief description of the isotope-enabled
184 POP2 and CLM5.0 models is provided below.

2.2.1 Ocean model: POP2/MARBL

186 POP2 are run on the standard model grid with 60 vertical layers and a horizontal resolution of
187 about 1° and finer resolution around the equator. The marine biogeochemical cycle is based on
188 the Biogeochemical Elemental Cycling (BEC) model (Moore et al., 2004;Moore et al., 2002) and
189 handled by the Marine Biogeochemistry Library (MARBL). It represents the cycling of carbon,
190 the carbon isotopes ^{13}C and ^{14}C, nitrogen, phosphorus, iron, silica, oxygen, and alkalinity. Carbon
191 isotopes are exchanged between the seven tracers: dissolved inorganic carbon (DIC), dissolved
192 organic carbon (DOC), calcium carbonate (CaCO$_3$), and three different phytoplankton (small
193 phytoplankton, diatoms, diazotrophs) and one zooplankton pool.

194 The net air-to-sea gas flux of CO$_2$, $F_{a,s,\text{net}}$, is modeled as the product of the piston velocity and the
195 difference between the saturation, C_{sat}, and surface water, C_s, concentration of dissolved CO$_2$
196 following Wanninkhof (2014):

$$197 \quad F_{a,s,net} = (1 - a_{ice}) \cdot a \cdot u_{10}^2 \cdot \left(\frac{660}{Sc_{CO2}}\right)^{-0.5} \cdot (C_{sat} - C_s) = k \cdot (C_{sat} - C_s) \qquad (2)$$

198   a_{ice} is the fraction of a grid cell covered by ice, a is a scaling factor, u_{10} is the wind speed at 10 m

199   above sea level, and Sc_{CO2} the Schmidt number of CO_2, and k the piston velocity with respect to

200   the liquid phase. A similar approach is used for computing the air-to-sea gas fluxes of the

201   isotopes of CO_2. The scaling factor a is set to 0.251 cm h^{-1} /(m s^{-1})^2 as in Wanninkhof (2014),

202   substantially lower than the value of 0.31 cm h^{-1}/(m s^{-1})^2 assumed by Jahn et al. (2015). This

203   downward revision of the piston velocity is broadly in agreement with earlier re-assessment of

204   the bomb-produced radiocarbon distribution within the ocean (Müller et al., 2008;Sweeney et al.,

205   2007;Peacock, 2004). The value of the coefficient a of 0.251 cm h^{-1} /(m s^{-1})^2 was derived using

206   the Cross-Calibrated Multi-Platform (CCMP) wind product at 0.25° and 6-h resolution

207   (http://podaac.jpl.nasa.gov/datasetlist?search = ccmp) by matching observations of bomb DI^{14}C

208   in an inverse ocean transport model approach (Wanninkhof, 2014). We note that the value of a is

209   tied to the applied wind product and its use with other wind products may lead to different air-sea

210   fluxes and, in turn, bomb ^{14}C inventory and Δ^{14}C values.

211   ^{14}C is, as ^{13}C and carbon, cycled between the atmosphere and ocean and between all marine

212   ecosystem carbon pools. Fractionation of ^{13}C versus ^{12}C is implemented, as described by Jahn et

213   al. (2015), following Zhang et al. (1995) for air-sea gas exchange and following Laws et al.

214   (1995) for photosynthesis, and fractionation of 2 ‰ is assumed for the formation of calcium

215   carbonate. Fractionation for ^{14}C is twice as large as for ^{13}C. Besides, a so-called "abiotic" ^{14}C

216   tracer is implemented in POP2 (Jahn et al., 2015). Abiotic ^{14}C does not cycle through the organic

217   matter pools and the fractionation factors for air-sea gas exchange fluxes are set to unity. The

218   abiotic implementation is a simplification, but requires much less computing resources than the

219   biotic implementation. We will compare simulated Δ^{14}C between the two implementations to test

220   the validity of the abiotic implementation. ^{14}C decays in POP2 with a half-life of 5730 years. We

221   note that the value of the half-life has recently been updated based on new measurements to 5700

222   years (Orr et al., 2017), but this small revision has not yet been implemented in CESM. The

223   standard ratios for ^{13}C/^{12}C and ^{14}C/C are set to unity in the POP2 model. Model units are

224   converted by applying the standard ^{14}C/C ratio of 1.176 10^{-12} for the computation of ^{14}C

225   inventories.

226

227

2.2.2 Land model: CLM5.0

CLM5.0 represents terrestrial carbon and nitrogen dynamics and features various vegetation, litter, and soil organic matter pools (Oleson et al., 2013). Each grid cell is covered by different land-use classes. Each class has its own set of plant functional types (PFTs) and soil columns. Vegetation is described by 15 different PFTs which either follow the C3 or C4 photosynthesis pathway. Twenty carbon (C) pools per PFT store C in vegetation. C is tracked for leaf, live stem, dead stem, live coarse root, dead coarse root, and fine root pools and corresponding storage pools representing, respectively, short-term and long-term storage of nonstructural carbohydrates. Decomposition of fresh litter material into progressively more recalcitrant forms of soil organic matter is formulated as a cascade of transformations between decomposing coarse woody debris, three litter, and three soil organic matter pools. These pools are vertically resolved by 10 layers over a depth of 3.8 m. Discrimination of ^{13}C is implemented following (Farquhar et al., 1989) considering kinetic fractionation during the diffusion of CO_2 across the leaf boundary layer and into the stomata and during enzymatic fixation for C3 plants. Unlike in POP2, ^{14}C fractionation is not explicitly considered and CLM carries fractionation corrected ^{14}C. The standard ratio for ^{13}C/^{12}C and ^{14}C/C are set to 0.0112372 and 10^{-12} in CLM5.0. Model results in gram-^{14}C are converted by multiplication with $1.176 \cdot 14/12.011 = 1.3707$ to compute ^{14}C inventories with 1.176 representing the ratio between the real and the model standard ratio, and 14 g/mol and 12.011 g/mol the molar mass of ^{14}C and C, respectively. ^{14}C decays in CLM5.0 with a half-life of 5730 years.

2.3 Setup of simulations

Eight simulations were performed. These include a spin-up (SPIN) as well as a simulation over the historical period 1850 to 2015 (HIST) and an associated 165-yr control run (CTRL) for both the land biosphere (LN) and the ocean-sea ice components (OC) with NYF. In addition, POP2 was run with an alternative climate forcing (JRA55) over the historical period and in a corresponding control.

Spin up and control runs were forced with 1850 conditions for atmospheric CO_2 (284.7 ppm), δ^{13}C (-6.61 ‰), and Δ^{14}C; prescribed atm. Δ^{14}C is distinguished between 3 latitudinal bands (>30ºN: -2.3‰; 30ºS-30ºN: -4.0‰; < 30ºS: – 5.8‰) following Graven et al. (2017). The

257   historical period simulation is forced with prescribed, transient atmospheric CO_2, $\delta^{13}C$, and $\Delta^{14}C$

258   following Meinshausen et al. (2017) and Graven et al. (2017).

259   In the code provided by NCAR, atmospheric ^{14}C boundary values are read from input files.

260   However, atmospheric boundary values are expected in units of $\delta^{14}C$ for the ^{14}C tracer in POP2,

261   whereas atmospheric boundary values are expected in units of $\Delta^{14}C$ for the abiotic ^{14}C tracer in

262   POP2 and by CLM5. We revised the code to account for this difference between $\delta^{14}C$ and $\Delta^{14}C$

263   of around 37‰ $(2 \cdot (\delta^{13}C+25) \approx 2 \cdot (-6.6+25))$.

264   The land component was forced with data from the Global Soil Wetness Project (GSWP3)

265   (Dirmeyer et al., 2006) which provides data from 1901 onwards. Spin up (SPIN_LN), control

266   simulation (CTRL_LN), and the first 50 years of the historical period simulation (HIST_LN)

267   were forced by repeatedly prescribing the climate data for the period 1901 to 1920. The GSWP3

268   climate data for 1901 to 2015 were prescribed for the same period in HIST_LN. Land use is

269   prescribed following the Land Use Harmonized version 2 data set (Hurtt et al., 2020).

270   The ocean model was forced with the Coordinated Ocean Research Experiments (CORE.v2)

271   Normal Year Forcing (NYF; Large and Yeager (2009)) during simulation SPIN_OC, CTRL_OC,

272   and HIST_OC. Climate data from the Japanese Reanalysis project (JRA55, Kobayashi et al.

273   (2015)) were used in a sensitivity simulation over the historical period (HIST_OC_JRA) and a

274   corresponding control run (CTRL_OC_JRA). The NYF and JRA55 data allow us to investigate

275   the influence of two different wind products and related changes in the piston velocity on

276   simulated bomb ^{14}C. NYF data are repeated annually. The JRA55 data cover the period from

277   1958 onwards. The JRA55 data capture the influence of global warming while allowing us to

278   prescribe a relatively constant climate in CTRL_OC_JRA and for the pre-1958 period in

279   HIST_OC_JRA. Specifically, the first twenty years of JRA55 (1958 to 1977) are applied

280   repeatedly in the simulations CTRL_OC_JRA. Similarly, the first twenty years of JRA55 data are

281   applied repeatedly during the years 1850 to 1957 in HIST_OC_JRA, followed by the JRA55 data

282   for the post-1958 period. The global mean surface air temperature in JRA55 varies within $\pm0.2^{\circ}C$

283   in the control and the pre-1958 period of HIST_OC_JRA. This is followed by global warming of

284   about $0.7^{\circ}C$ over the period 1958 to 2015, mainly realized after 1989, in HIST_OC_JRA.

285   SPIN_LN was started using the initial files downloaded from NCAR and run for 750 years.

286   CTRL_LN and HIST_LN were continued from the end of SPIN_LN. The remaining model drifts

287   in global carbon and radiocarbon are small after the spin-up. Global vegetation carbon remains

288   constant and the global soil carbon inventory changes by less than 1 GtC or about 0.5‰ over the

289   control simulation. Δ^{14}C of vegetation carbon remains constant during the control CTRL_LN.

290   Drift in Δ^{14}C are typically modest for soil carbon ($< \pm 2$‰/century, except in northern Siberia and

291   Canada and parts of the Sahara, where Δ^{14}C of soil carbon shows a substantial drift as these soils

292   continue to age. The total ecosystem ^{14}C inventory decreases from 251 kmol to about 249 kmol

293   over the control simulation.

294   SPIN_OC was started using the initial files downloaded from NCAR and run for 1350 years.

295   Initial values for ^{14}C and ^{13}C are missing in the files from NCAR and these missing values were

296   specified as follows. δ^{13}C of DIC was prescribed following the gridded, observation-based

297   preindustrial distribution of Eide et al. (2017); δ^{13}C values for the top 200 m are missing in the

298   Eide et al. data and were set to the values at 200 m depth. δ^{13}C of DOC is set to -20 ‰. ^{14}C of

299   DIC is initialized using the information for abiotic Δ^{14}C in the NCAR initial files. We apply

300   equation 1b) with δ^{13}C=0 to set $\delta^{14}C_{biotic} = (\Delta^{14}C_{abiotic} + 50)$ /0.95. Δ^{14}C of DOC is set to -100 ‰.

301   SPIN_OC was stopped in year 675 to adjust the isotopic carbon pools of DIC and DOC to speed

302   up equilibration. The difference in the isotopic pools between years 675 and 475 was added to the

303   pools. In other words, the trend over years 475 to 675 was extrapolated for another 200 years.

304   SPIN_OC was then continued for another 675 years with the updated isotopic concentrations.

305   At the year 1350, there were still trends in most ocean variables. Trends are typically modest in

306   the upper ocean and more substantial in the deep ocean. The mean ocean trend in Δ^{14}C is -0.32‰

307   per century and horizontally-average trends are between -5‰/century in the deep Pacific and

308   +3‰/century in the upper Pacific and smaller for other basins. The trends in the upper ocean are

309   small in comparison to the anthropogenic ^{14}C and Δ^{14}C changes simulated in HIST_OC and

310   HIST_OC_JRA.

311

312

2.4 Drift correction

We correct the results from historical runs (HIST_LN, HIST_OC, HIST_OC_JRA) for long-term trends by subtracting the drift from control runs (CTRL_LN, CTRL_OC, CTRL_OC_JRA). For example, the change in a variable at time *t* is estimated by the difference in the results from HIST_OC(t) and CTRL_OC(t). The bomb radiocarbon inventory is evaluated as follows for both the ocean and the land:

$$^{14}I_{bomb}(t) = [^{14}I_{IND}(t) - {}^{14}I_{IND}(t = 1945)] - [^{14}I_{CTRL}(t) - {}^{14}I_{CTRL}(t = 1945)], \tag{3}$$

where $^{14}I_{bomb}(t)$ represents the change in ocean ^{14}C inventory since 1945. This change is mainly driven by the ^{14}C production from atomic bomb tests but is also influenced by other small anthropogenic ^{14}C sources, as well as the impact of fossil fuel burning, land use, and climate change.

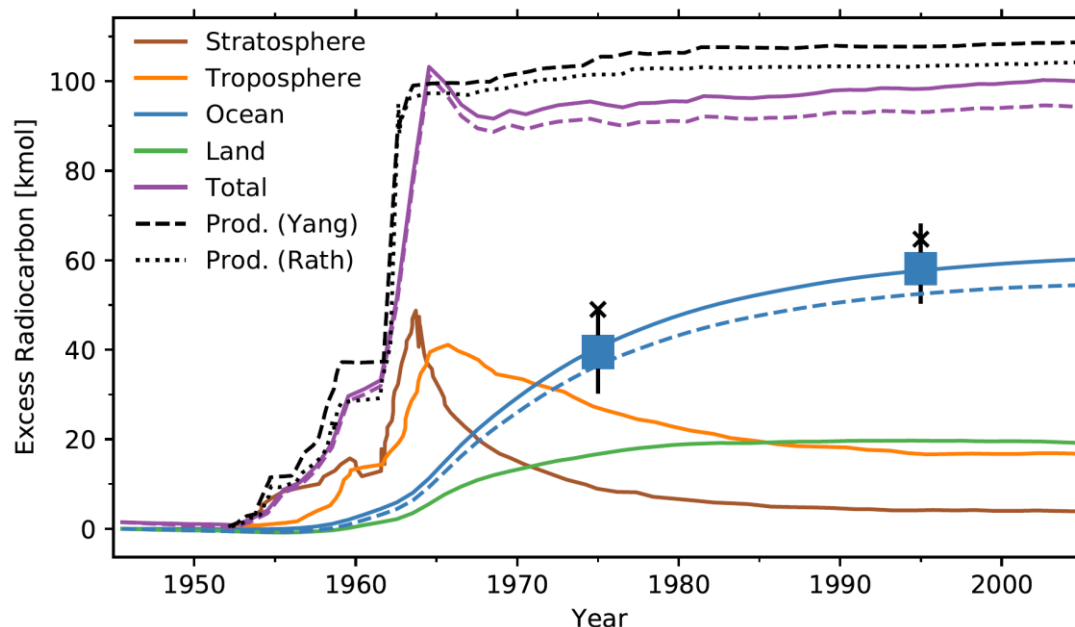**2.5 Establishing the global budget of excess ^{14}C**

The transient evolution in the Earth system inventory of excess ^{14}C is estimated from the sum of the land and ocean excess ^{14}C inventories simulated by CLM5.0 and POP2 plus the tropospheric and stratospheric excess ^{14}C inventories estimated from measurements of $\Delta^{14}C(CO_2)$, $\delta^{13}C(CO_2)$, and CO_2 on atmospheric samples as described by Naegler and Levin (2009a).

The two excess ^{14}C production records of Naegler and Levin are estimated from the compilations of atomic bomb test explosions by Yang et al. (2000) or Rath (1988) and cover the bomb period up to 2004. These compilations are scaled to match an estimate of the total bomb ^{14}C inventory in the mid-1960s. The contribution of the ^{14}C release by the nuclear industry is included in these production records. The uncertainty in cumulative production up to 1980 is estimated to be around 6 kmol ^{14}C and the uncertainty in the stratospheric inventory to about 2 to 2.5 kmol ^{14}C, with additional smaller uncertainties associated with natural ^{14}C productivity, the release by the nuclear industry, and the tropospheric ^{14}C inventory (Naegler and Levin, 2009a, 2006). Any difference between the Earth system inventory and the cumulative production of excess ^{14}C represents an accumulated budget imbalance. Imbalances larger than uncertainties in the atmospheric and production data, point to a mismatch in simulated uptake of ^{14}C from the atmosphere by POP2 and CLM5.

3 Results

3.1 The global budget of bomb ^{14}C

Figure 1: The Earth system budget of excess radiocarbon: observational estimates versus model results. The evolution of ^{14}C inventories are shown for the stratosphere (brown), troposphere (orange), ocean (blue), and land biosphere (green). Their total (magenta) is compared to two estimates of the excess ^{14}C production (black; dotted, dashed). Data for the ocean and land biosphere are from simulations with POP2 and CLM5. Dashed blue and dashed magenta show results obtained with the JRA55 instead of NYF in POP2. The ocean bomb ^{14}C inventories simulated by Jahn et al. (2015) are indicated by crosses. All other data are from Naegler and Levin (2009a). The range of best estimates (Sweeney et al., 2007;Peacock, 2004;Müller et al., 2008;Key et al., 2004) for the ocean inventory for 1975 and 1995 is given by the filled box and the bar represents the overall uncertainty of these estimates as summarized by Naegler and Levin (2009a). Production records are extrapolated from 2004 to 2010.

We first address the Earth system budget of bomb ^{14}C to evaluate the combined bomb ^{14}C model flux to the ocean and land. Estimates of cumulative production are compared to the Earth system inventory of excess ^{14}C in Fig. 1. The change in the Earth system ^{14}C inventory, determined by the sum of modeled ocean and land biosphere uptake plus observation-based tropospheric and stratospheric inventory changes, is generally lower than estimates of the bomb ^{14}C production (magenta versus black lines in Fig. 1).

Both cumulative production records show a steep increase to 96-99 kmol until 1963, when the bomb-test ban treaty was set in place, followed by a modest increase of 7 kmol until 1980, and

361 near-constant values after 1980. The estimate based on Rath remains around 4 kmol lower than

362 the estimate based on Yang after 1963.

363 The stratospheric and tropospheric bomb inventory strongly increased in the 1950s to peak at 49

364 kmol in 1963 and 41 kmol in 1965. Afterward, the stratospheric inventory declined steeply, to 14

365 kmol in 1970 and 4 kmol in 2005, while the tropospheric inventory shows a more gradual decline

366 to 17 kmol in 2005. Modeled land and ocean uptake of bomb ^{14}C are largest in the 1960s. The

367 land inventory is 14 kmol in 1970, further increases to 19 kmol in 1980 and remains roughly

368 stable thereafter. The ocean inventory is 30 kmol in 1970, further increases to 48 kmol in 1980

369 and reaches 59 kmol in 2000. The modeled inventory is lower when POP2 is forced with the

370 JRA55 instead of the NYF and the difference between the two simulations grows to about 5.5

371 kmol at 2000.

372 The total Earth system inventory of excess ^{14}C reproduces the rapid initial increase in cumulative

373 production of around 100 kmol ^{14}C, though with a delay of a few years. The Earth system

374 inventory peaks in 1964 and declines in the next three years by about 10 % from 103 to 92 kmol.

375 This is in contrast to the cumulative production records that show little changes in this period.

376 Afterward, the inventory follows the evolution of the cumulative production records, albeit at a

377 lower absolute value. The combined bomb ^{14}C inventory shows an offset of 4 to 7 kmol to the

378 cumulative production record based on Rath and of about 9 kmol to the record based on Yang

379 during the period 1970 to 2005. In this period, the change in total production (5 to 7 kmol) and

380 the change in the Earth system inventory (7.5 kmol) remain small and comparable. Thus, the

381 budget imbalance mainly accrues before 1970. The accumulated budget imbalance of 4 to 7 kmol

382 (Rath) and of about 9 kmol (Yang) is also similar or larger than the uncertainty in the cumulative

383 production record of 6 kmol. The budget imbalance is larger when the total inventory is

384 determined using results from the POP2 simulations with JRA55 forcing (dashed, magenta in Fig.
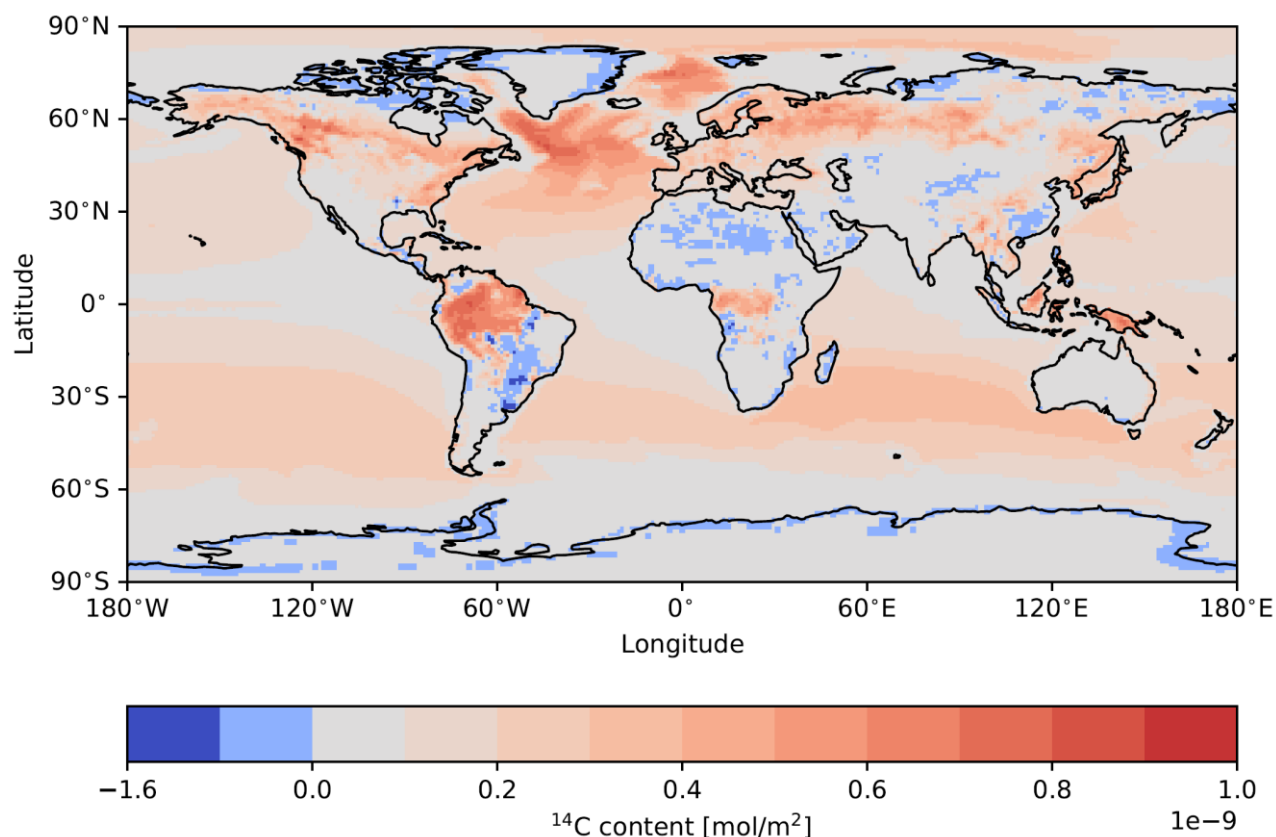
385 1) instead from the simulation with NYF.

386 The differences between the ^{14}C production records and the Earth system inventory estimates

387 suggest that the simulated uptake of excess ^{14}C from the atmosphere is underestimated. This is

388 primarily the case during the 1960s when simulated ocean and land uptake is the largest. After

389 1970, the accumulated budget imbalance does not further increase and the combined modeled

390 land and ocean uptake is consistent with the observational records. A too low combined uptake

391 by POP2 and CLM5 in the 1960s could explain the delay in increase between the production and

392 total inventory in the early 1960s and the offset between inventory and cumulative production

393 after 1970 when uncertainties in the atmospheric inventory become small.

394 We now discuss potential reasons for the decline in the Earth system inventory between 1964 and

395 1967 (Fig. 1 magenta line). Production from bomb tests is small during this short period. The

396 decline by 12 kmol is either due to a too low simulated ^{14}C uptake from the atmosphere by CLM5

397 and/or POP2 or a too large decline in the atmospheric inventory as reconstructed from

398 observations, or a combination of these factors. The simulated ocean uptake over these 3 years

399 would need to be more than doubled to avoid the decline. Such a large upward revision would not

400 be compatible with marine ^{14}C observations because modeled and observation-inferred bomb ^{14}C

401 inventories closely agree and uncertainties in observational estimates are about 20% (Fig. 1 blue

402 symbols and line). Simulated land uptake amounts to 5 kmol over these three years and would

403 need to be more than tripled to avoid the decline. Therefore, it is difficult to explain the decline

404 by shortcomings of CLM5 alone. The prescribed atmospheric inventory declines by 27 kmol

405 from 1964 to 1967. Most of this decline is realized in the stratosphere. Uncertainties in the

406 stratospheric inventory arise from sparse sampling and large spatio-temporal variations in

407 stratospheric ^{14}C concentrations, while the tropospheric inventory is well known. However, the

408 decline of 12 kmol is substantially larger than the uncertainty (2-2.5 kmol) given for the

409 stratospheric inventory data (Naegler and Levin, 2009a, 2006). A scenario that would avoid the

410 decline in the Earth system ^{14}C inventory and the related budget imbalance during the period

411 1964 to 1967 likely needs to combine a downward revision of the stratospheric decline and an

412 upward revision of modeled CLM5 land biosphere uptake and, perhaps to a lesser extent, of

413 POP2 ocean uptake. The inferred decline provides further evidence that the simulated ^{14}C uptake

414 from the atmosphere is too low during the 1960s. Importantly, this evidence for too low uptake is

415 independent of the production records and associated uncertainties.

416 During the 1950s, the uptake of bomb ^{14}C from the atmosphere is relatively small, because the

417 changes in tropospheric Δ14C were rather modest, and the Earth system inventory is in good

418 agreement with the inventory record based on Rath. The small land and ocean uptake imply that

419 remaining budget imbalances during this early period are likely due to uncertainties in the

420 production and atmospheric data. In summary, the combined uptake by POP2 and CLM5 is too

421 low during the 1960s, while the combined uptake over the period 1970 to 2004 is consistent with

422 production estimates and atmospheric data.

Figure 2: Changes in the ^{14}C column inventory in the ocean and on land from 1945 to 1995 simulated by POP2 with normal year forcing (HIST_OC) and CLM5 (HIST_LN).

3.2 Excess ^{14}C in the POP2 ocean model

3.2.1 The global ocean bomb ^{14}C inventory

Next, we assess whether the Earth system budget imbalances arise from ocean model biases. The global ocean bomb ^{14}C inventory simulated by POP2 agrees well with observation-based estimates (Fig.1 blue line vs symbols). POP2, driven by NYF, simulates an ocean inventory of 41.3 kmol in 1975 and 57.9 kmol in 1995. These estimates are well within the range of recent central estimates of the ocean's excess ^{14}C inventory of 36 to 44 kmol (overall uncertainty range: 30.3 kmol to 49.3 kmol) for 1975 (Müller et al., 2008;Sweeney et al., 2007;Peacock, 2004) and 54.5 to 62 kmol (overall uncertainty range: 52 to 68 kmol) for 1995 (Sweeney et al., 2007;Müller et al., 2008;Peacock, 2004). This good agreement between POP2 and observational estimates suggests that the budget imbalances discussed in the previous section are likely not caused by too low modeled ocean uptake, but rather linked to too low uptake by the land biosphere.

438   The good agreement between the observation-inferred inventories and POP2 results supports the

439   representation and time scales of air-sea gas transfer and surface-to-thermocline transport on the

440   global scale for POP2 with NYF. The air-sea flux of bomb ^{14}C is given by the piston velocity

441   multiplied by the perturbed air-sea gradient in dissolved $^{14}CO_2$ (Eq. 2). The global ocean uptake

442   of bomb ^{14}C before the first global survey of ^{14}C by the Geochemical Ocean Section Study

443   (GEOSECS, 1972 to 1978) primarily depends on the magnitude of the piston velocity, whereas

444   uncertain ocean transport has a marginal influence on the large air-sea $^{14}CO_2$ gradient during the

445   time of the bomb peak (Müller et al., 2008;Siegenthaler, 1989). Thus, the GEOSECS bomb ^{14}C

446   data provide a particularly strong constraint on the piston velocity. On the other hand,

447   uncertainties in the overturning time scales within the ocean become important for the modeled

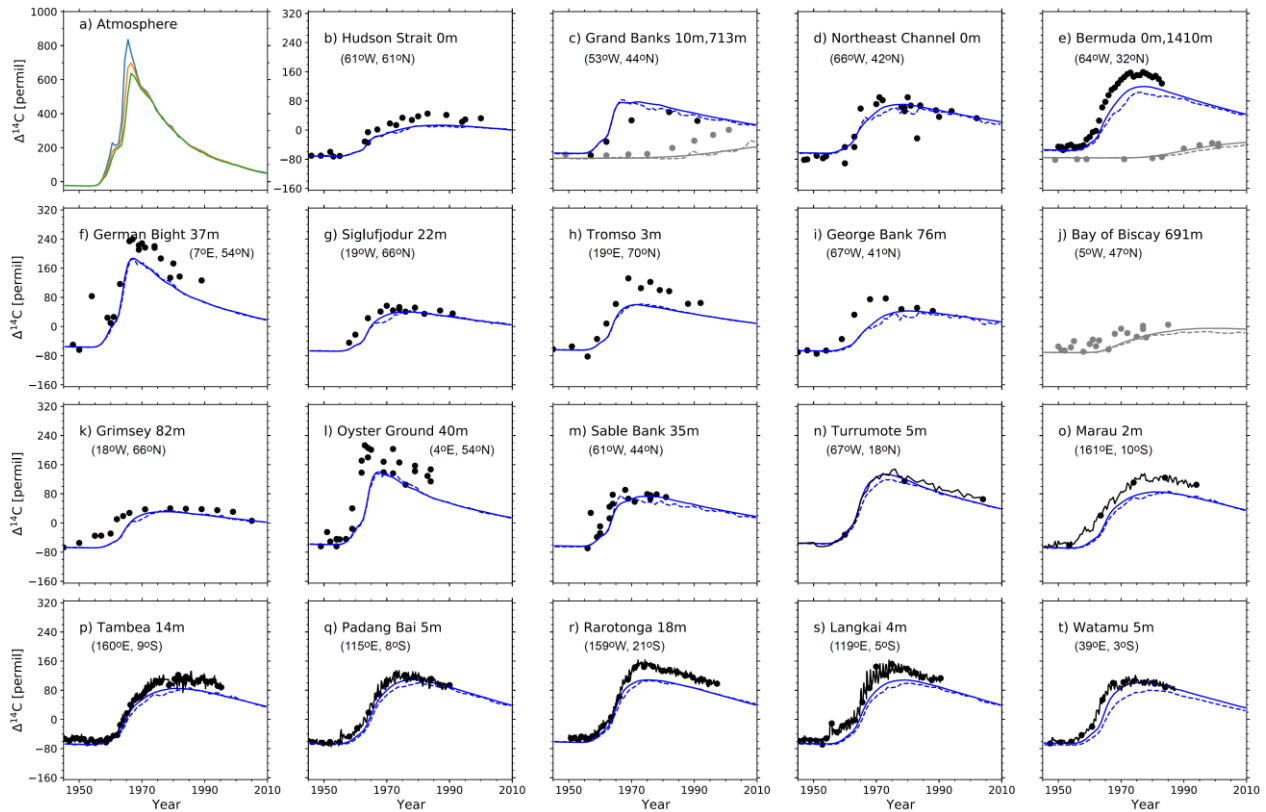448 ^{14}C uptake during more recent decades and the model inventory in 1995.

449   The ocean ^{14}C uptake appears biased low when POP2 is forced by JRA55 instead of NYF (Fig 1,

450   blue dashed line). The simulated uptake is only 35.7 kmol for 1975 and 52.3 kmol for 1995. Both

451   values are in the lower half of the observational range and at or below the central estimates from

452   different studies. As discussed in the previous section, the budget imbalance is considerably

453   larger when JRA55 instead of NYF is applied in POP2. These results suggest that the piston

454   velocity in the POP2 stand-alone model version with JRA55 forcing is likely too low on the

455   global scale, though uncertainties in the observational ocean inventory estimates remain. Further,

456   ocean circulation is also different under JRA55 NYF and this may contribute to the low bomb ^{14}C

457   inventory simulated for 1995 with JRA55 forcing.

458   Regionally, the highest column inventories of bomb ^{14}C are simulated in the North Atlantic (Fig.

459   2). Column inventories are also high in the mid-latitude Southern Hemisphere, where Antarctic

460   Intermediate Water and Subantarctic Mode Water (Talley, 2013) efficiently transports excess ^{14}C

461   to depth. Column inventories are low in the tropical upwelling regions, around Antarctica, and in

462   the northern North Pacific.

463   **3.2.2 The coral Δ^{14}C records**

464   Next, we evaluate POP2 performance by comparing the simulated evolution of Δ^{14}C(DIC) with

465   Δ^{14}C records from corals and bivalves in the North Atlantic, tropical Pacific, and Indian Ocean

466   (Fig. 3). The proxy data show a rapid Δ^{14}C increase during the 1960s in surface waters. Peak

467   surface Δ^{14}C values are reached in the late 1960s and early 1970s, followed by a slow decline.

468   The amplitudes in surface $\Delta^{14}C$ change between pre-bomb and peak values range between 85 and

469   250‰ (Fig. 3k, 3f).

470

Figure 3: Simulated evolution of $\Delta^{14}C(DIC)$ by POP2 (solid and dashed lines) versus $\Delta^{14}C$ records from corals and

bivalves (filled circles, filled circles with solid lines for high-resolution records (n)-t)). Model results are for the

simulation with NYF (solid) and JRA55 (dashed) forcing and represent annual means from the grid cell including the

sampling location and sampling depth (indicated in meters). Data and model results in the thermocline are shown in

grey. Data are from the North Atlantic as compiled by Dentith et al. (2019), Puerto Rico, Turrumote Reef (Kilbourne

et al., 2007), Solomon Islands, Marau (Schmidt et al., 2004), Solomon Islands, Tambea (Guilderson et al., 2004),

Lombok Street, Padang Bai (Guilderson et al., 2009), Rarotonga (Guilderson et al., 2000), Langkai, Makassar Strait

(Fallon and Guilderson, 2008), and off the coast of Kenya, Watamu (Grumet et al., 2002). The atmospheric

$\Delta^{14}C(CO_2)$ evolution is shown in panel a) for the northern hemisphere (> 30°N; blue), the tropics (orange), and the

southern hemisphere (<30°S; green); note different y-axis scale.

481   The model represents the pre-bomb $\Delta^{14}C$ proxy data well and generally within the scatter of the

482   coral data in the surface North Atlantic, with exceptions at Grand Banks (Fig. 3c) and Northeast

483   Channel (Fig. 3d), where model data are about 20‰ higher, and at Bermuda (Fig. 3e), where

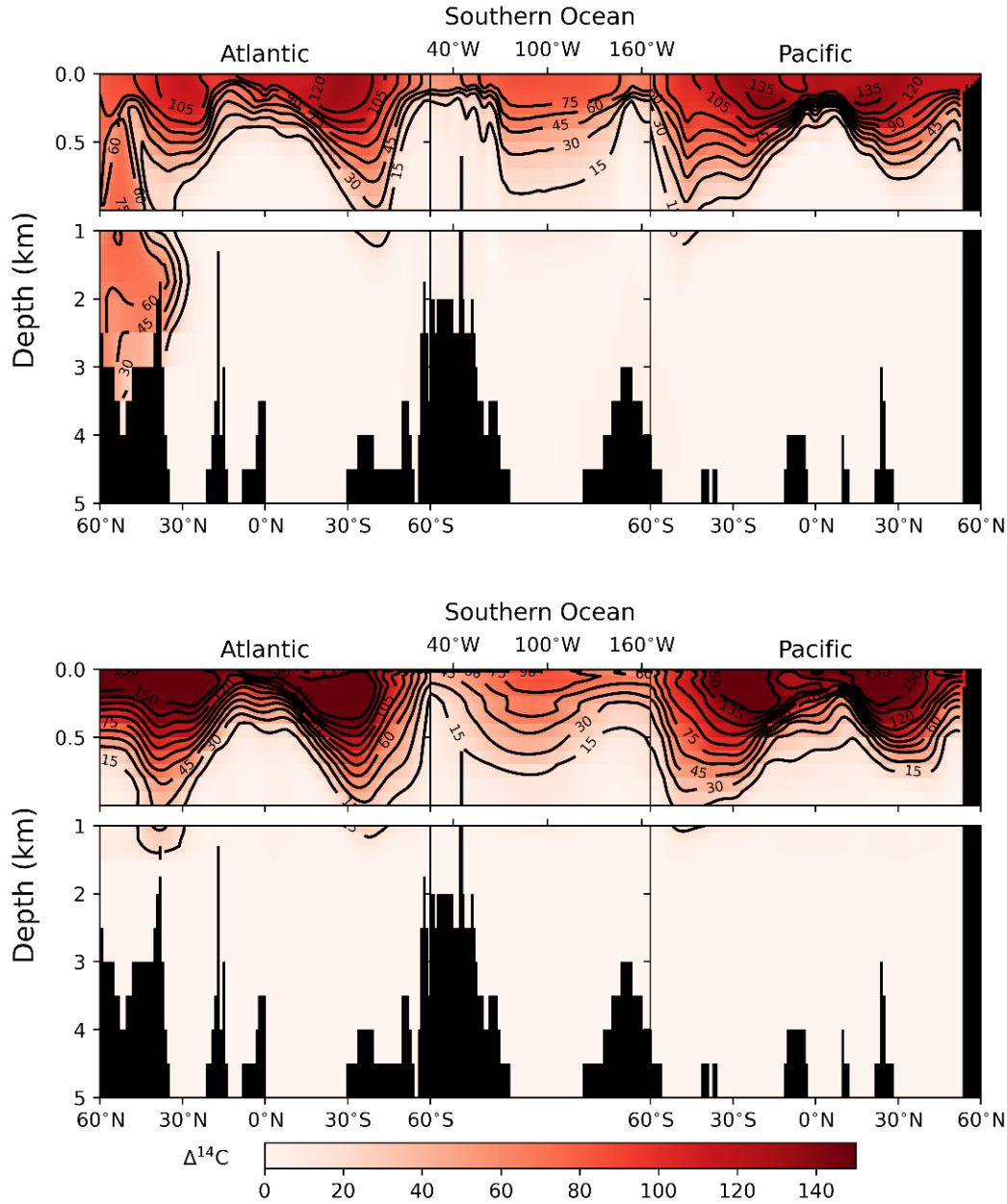484   model data are about 10‰ lower than most coral data. Pre-bomb $\Delta^{14}C$ simulated by POP2 is

485   typically about 10 to 15‰ lower than the $\Delta^{14}C$ proxy data from the Pacific and the Indian Ocean

486   (Fig. 3o to 3t).

487   The increase in surface $\Delta^{14}C$ during the bomb-test period is underestimated in magnitude at all

488   locations by POP2 compared with the proxy data. In the North Atlantic, proxy peak values are

489   matched within 20‰ at five stations, within 40‰ at eight stations and within 75‰ at all of the 12

490   surface locations (Fig 3b, to 3h). Deviations in peak surface $\Delta^{14}C$ range from a few permil to up

491   to 60‰ in the Indian and Pacific surface locations (Fig 3o to 3t). The evolution of $\Delta^{14}C$ at depth

492   is within the scatter of the coral data at Bermuda (32°N) and a depth of 1410 m (Fig. 3e, grey)

493   and the Bay of Biscay (46 °N) at 691m (3j) and underestimated at Grand Banks (44 °N) at 713 m

494   (3c). Peak $\Delta^{14}C$ values from the POP2 simulation with JRA55 wind forcing are similar to those

495   obtained with NYF at mid and high latitudes in the North Atlantic, but typically lower than for

496   NYF at Bermuda and Puerto Rico and in the low latitude Pacific and Indian locations. $\Delta^{14}C$ at

497   pre-bomb times and after 1990 are generally indistinguishable for the POP2 model setups.

498   The deviation between proxy and model data may arise due to a misrepresentation of piston

499   velocity or ocean transport processes in POP2 or a representation bias by comparing proxy data

500   sampled close to the coasts with grid cell values representing open ocean waters in POP2. We are

501   not in a position to distinguish these different factors. The lower than observed pre-bomb and

502   peak $\Delta^{14}C$ values in the low latitude Indian and Pacific may point to a too strong upwelling of

503   thermocline waters in POP2 and/or a too sluggish gas transfer at these locations.

504   **3.2.3 The spatial distribution of bomb $\Delta^{14}C$ in the ocean**

505   The modeled spatial distribution of bomb $\Delta^{14}C$ is compared with observational estimates (Key et

506   al., 2004) along a transect through the Atlantic, Southern Ocean, and Pacific (Fig. 4). The

507   mapped observational data are derived from samples taken in the 1980s in the Atlantic, while

508   model output is from the year 1995, representative for the Pacific and Southern Ocean data. The

509   different sampling periods call for caution when comparing model and gridded data in the North

510   Atlantic. The model represents the main features with shallow penetration of the bomb signal

511   around the equator, deep penetration in the regions of intermediate and mode water masses, and

512   intermediate penetration in the Southern Ocean.

Figure 4: (a) Modeled versus (b) observation-based distribution of "bomb" Δ^{14}C. Model results represent the difference in Δ^{14}C between the historical period simulation HIST_OC with Normal Year Forcing at 1995 CE and the corresponding year in the control simulation CTRL_OC. Observational data are from the gridded data product of the Global Ocean Data Analysis Project for Carbon (GLODAP) (Key et al., 2004). Results are shown for a section through the Atlantic at 25°W, through the Southern Ocean westward from 25°W to 175°W at 60°S, and through the Pacific at 175°W. Observational bomb ^{14}C maps were calculated only for the upper 1500 m by Key et al. Note that the mapping in the North Atlantic is based on samples taken between 1981 and 1983, and thus 12 to 14 years earlier than the model output.

523 Focusing on the 15‰ isoline, we find a good model-data agreement. The deepest occurrence of

524 the 15‰ isoline in the South Atlantic is around 1300 m at 38°S in the GLODAP mapping and at

525 41°S in POP2. Its depth varies along 60°S between 160 m and 790 in GLODAP and between 160

526 m and 880 m in POP2. In the South Pacific, its deepest location is at 54°S and a depth of 1100 m

527 (GLODAP) and 1300 m (POP2), respectively. The maximum and minimum depth of the 15‰

528 isoline is similarly matched in the North Pacific. In the equatorial Pacific, however, this isoline is

529 simulated at 400 m in POP2 and about 200 m shallower than in GLODAP. This may point to too

530 vigorous equatorial upwelling in POP2 in the Pacific.

531 The bomb Δ^{14}C signal is simulated to reach near-bottom waters around 40 °N to 60 °N in the

532 North Atlantic. However, Key et al. mapped bomb Δ^{14}C only to a depth of 1500 m and from

533 samples taken in the early 1980s, while model results are displayed for 1995. The modeled deep

534 penetration of the bomb ^{14}C signal in the high latitude Atlantic is consistent with the observed

535 penetration of bomb-produced tritium, CFCs, and anthropogenic carbon in this area (Perez et al.,

536 2018;Danabasoglu et al., 2009;Schlitzer, 2007;Sabine et al., 2004;Weiss and Roether, 1980), and

537 linked to North Atlantic Deep Water formation. It is also qualitatively consistent with the deep

538 penetration of bomb ^{14}C reconstructed by Broecker et al. (1995).

539 In summary, the overall good representation of the uptake and penetration of bomb ^{14}C by the

540 POP2 model under NYF is in line with the good agreement between observed and simulated

541 CFC-11 concentrations documented by Danabasoglu et al. (2009). The comparison shown in Fig.

542 4 implies that the time scales for the ventilation of the upper thermocline are reasonably well

543 captured by POP2. The good agreement between simulated and observation-based global ocean

544 bomb ^{14}C inventories at 1975 and 1995 suggests that the Earth system bomb ^{14}C budget

545 imbalance (Fig. 1) is likely not caused by deficiencies in ocean ^{14}C uptake simulated by POP2

546 with NYF. Rather the Earth system budget imbalance may be linked to too low uptake by the

547 land model CLM5.

3.3 Excess ^{14}C in the CLM5 land biosphere

549 In this section, we investigate the evolution of the globally integrated carbon and ^{14}C inventory of

550 vegetation and soils from 1850 to 2010 in more detail (Fig. 5a,b) and compare the simulated land

551 biosphere inventory of excess ^{14}C with the observational estimate of Naegler and Levin (2009a)

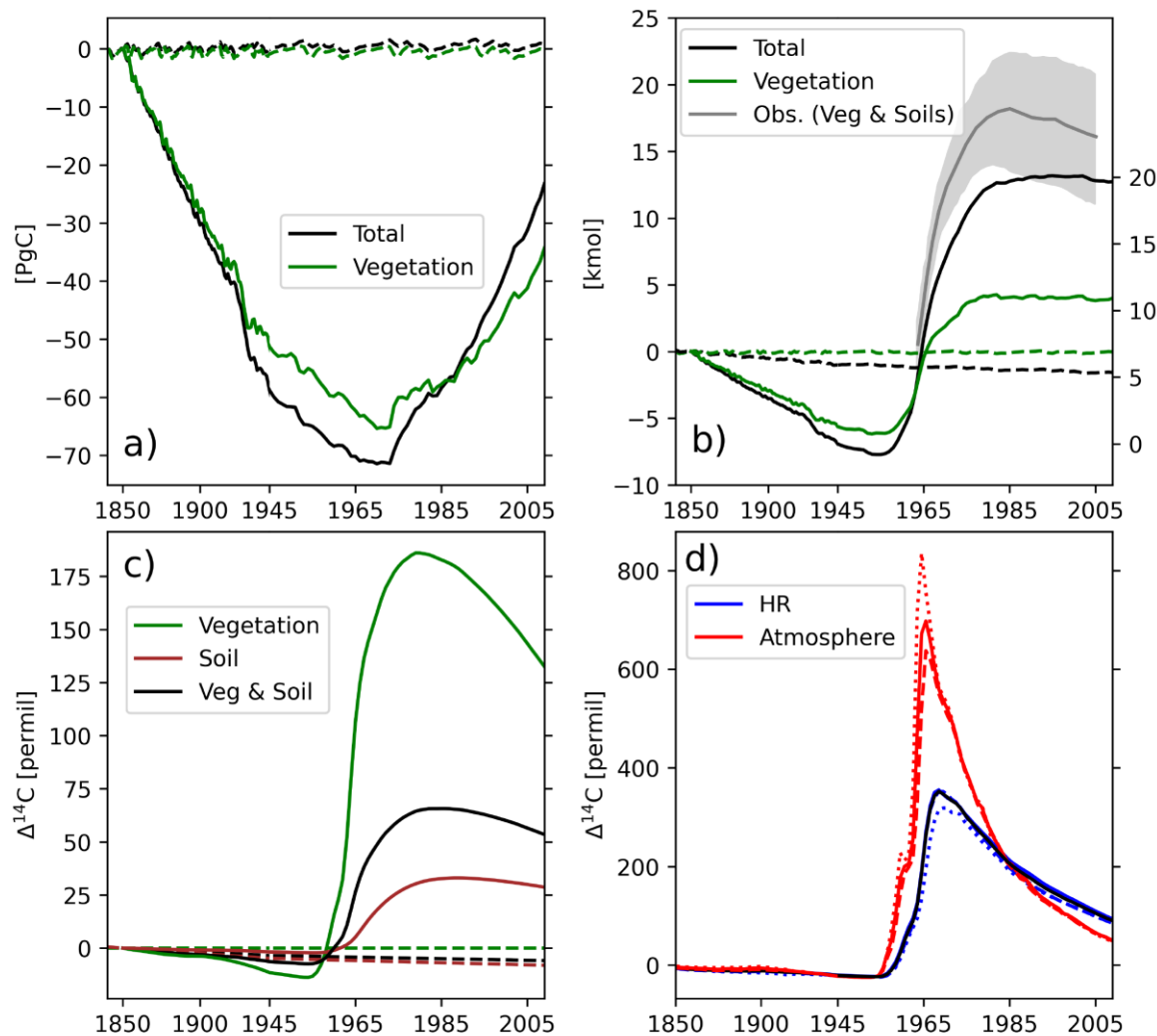552 (Fig. 5b, black line, and gray shading). We also briefly address the evolution of Δ^{14}C of

553   vegetation and soils (Fig. 5c), and heterotrophic respiration (Fig. 5d) as well as column

554   inventories of bomb ^{14}C on land (Fig. 2).

555   CLM5.0 simulates a terrestrial carbon release of 71 GtC over the period from 1850 to 1970 (Fig.

556   5a). Land-use emissions are larger than sink fluxes in this period. Afterward, the model simulates

557   a terrestrial carbon sink of 48 GtC until 2010. These changes are mainly driven by changes in

558   vegetation carbon. Soil carbon (difference between black and green line in Fig. 5a) decreased by

559   about 5 GtC until 1970 and increased by 16 GtC from 1970 to 2010.

560   The simulated global land biosphere turned from a ^{14}C source into a sink around 1960 (Fig. 5b).

561   The CLM5 land biosphere released ^{14}C in the 19th and early 20th century due to the loss of

562   carbon, discussed in the previous paragraph, and the slight decrease in atmospheric Δ14C (Fig 1d,

563   red lines) and gained ^{14}C, mainly in response to the atmospheric bomb Δ14C peak (Fig 1d).

564   Vegetation lost 5.8 kmol of ^{14}C between 1850 and 1960, gained about 10 kmol in the next 20

565   years and its ^{14}C inventory remained stable thereafter. The soil ^{14}C inventory changed little (-0.26

566   kmol) until 1960, increased by 8.1 kmol to peak around 1995, followed by a slight decline.

567   Most of the land uptake of excess ^{14}C is by forest ecosystems (Fig. 2). Typical bomb ^{14}C column

568   inventories are around 1×10^{-9} mol ^{14}C m^{-2} in forested areas, and of similar magnitude as the

569   column inventories in the northern North Atlantic. Deforestation caused local reductions in ^{14}C

570   inventories over the bomb period in several regions, including Brazil, tropical Africa, and East

571   Asia (Fig. 2).

572   Naegler and Levin (2009a) analyzed uncertainties in the bomb ^{14}C budget and constructed the

573   best estimate and the allowable range for the land biosphere bomb ^{14}C inventory for the period

574   after 1963 (Fig. 5b, grey line and shading, right y-axis). The bomb ^{14}C inventory, i.e., the

575   inventory change since 1945 simulated by CLM5.0 is below the lower bound of the range

576   constructed by Naegler and Levin before 1990 and 5.3 and 5.5 kmol lower than the reference

577   scenario of Naegler and Levin in 1970 and 1985, respectively (Fig. 5b). These results imply that

578   the cumulative uptake of bomb ^{14}C until 1970 is underestimated by CLM5 by about 25%. A 5

579   kmol higher bomb ^{14}C uptake over 1945 to 1970 by CLM5 would also reconcile the imbalance in

580   the Earth system budget discussed in section 3.1 for the period after 1970.

Figure 5: Changes in the global land biosphere simulated by CLM5. (a) Carbon inventory, (b) ^{14}C inventory, c) mean Δ^{14}C of vegetation (green), soils (red), and vegetation and soils (black), d) mean Δ^{14}C of heterotrophic respiration ('HR'; blue) and tropospheric CO_2 ('Atmosphere'; red) for 3 latitudinal belts (dotted: >30°N; solid: 30°S-30°N; dash < 30°S). The right y-axis in panel b) refers to changes in the total (soil and vegetation) inventories of ^{14}C in kmol relative to 1945 and permits one to compare the ^{14}C inventories simulated by CLM5 (black) with the observation-inferred estimate of Naegler and Levin (2009a) (grey solid: their reference; shading: range spanned by their upper- and lowermost estimates). Dashed lines in (a), (b), and (c) show changes in the control simulation as used to correct for model drift. Note different x-axis scaling before and after 1945.

Soil ^{14}C data suggest that modeled ^{14}C uptake by soils is high. Shi et al. (2020) report less negative Δ^{14}C and younger soil ages in CLM5 than measured in modern soils (Shi et al., 2020;He et al., 2016). In surface soils and for 2000 CE, over 60% of carbon had positive Δ^{14}C values compared with only about 14% of carbon in the gridded dataset (Shi et al., 2020). Positive Δ^{14}C

594   values must originate from the uptake of bomb ^{14}C. In other words, the higher than observed

595   Δ^{14}C in surface soils suggests that the surface soils of CLM5 absorb too much bomb ^{14}C.

596   Bringing simulated soil Δ^{14}C in agreement with soil Δ^{14}C observations, would probably lower

597   bomb ^{14}C uptake by soils and thus widen the discrepancy between the bomb ^{14}C uptake simulated

598   by CLM5 and the observational range given by Naegler and Levin (2009a). These considerations

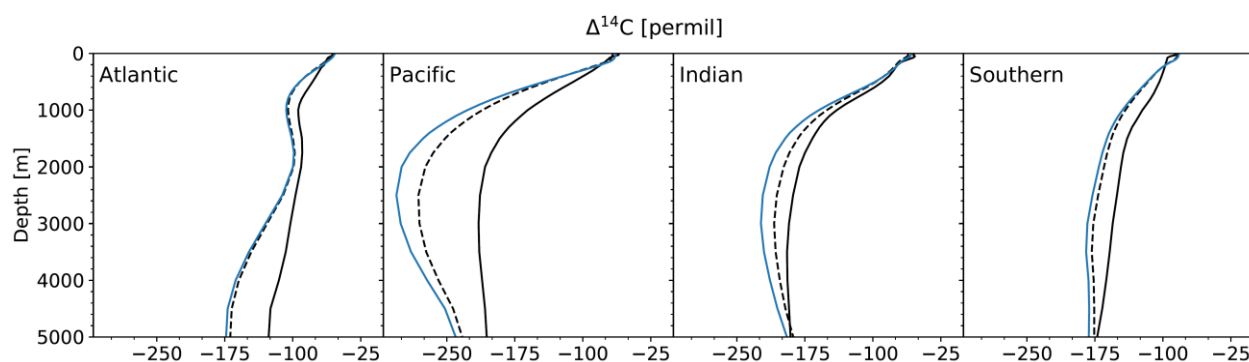599   imply that the uptake of bomb ^{14}C by vegetation is too low.

600   A change in the inventory of carbon causes a corresponding change in the ^{14}C inventory. The

601   release of carbon in the 19th and early 20th century and the carbon uptake in the late 20th century

602   is in line with results from a deconvolution of the atmospheric CO_2 record (Joos et al.,

603   1999;Friedlingstein et al., 2019). For the period 1970 to 2010, CLM5.0 yields a global land sink

604   of about 48 GtC, while the Global Carbon Budget suggests a sink of 41 GtC. This difference

605   translates into a small difference in the ^{14}C inventory of ~1 kmol ^{14}C. However, independent

606   evidence (Joos et al., 1999;Friedlingstein et al., 2019) suggests that the land biosphere turned into

607   a sink already around 1940 and not only around 1970 as in CLM5. The land biosphere absorbed

608   6±6 GtC and 10 GtC during the period 1945 to 1970 according to the observation-based estimate

609   of Joos et al. (1999) and the results from the Global Carbon Budget (Friedlingstein et al., 2019),

610   respectively. In contrast, CLM5.0 suggests a release of about 13 GtC in the same period. This

611   difference between modeled and estimated carbon uptake of 19 to 23 GtC transfers in an

612   additional uptake of ~2 kmol ^{14}C during the period 1945 to 1970. This additional ^{14}C would

613   contribute to lower the discrepancy between model-based ^{14}C inventory and production estimates

614   as discussed in sections 3.1 and would bring CLM5 results in better agreement with the reference

615   scenario for the land inventory of Naegler and Levin (2009a) (Fig. 5b).

616   Simulated changes in the Δ^{14}C signatures of vegetation, soil, and heterotrophic respiration are

617   briefly addressed. The Δ^{14}C signature of heterotrophic respiration, vegetation, and soils follows

618   the atmospheric Δ^{14}C forcing with a delay and with muted amplitude (Fig. 5c). Δ^{14}C of

619   heterotrophic respiration peaks at around 330‰ and a few years later than tropospheric Δ^{14}C. It

620   equals tropospheric Δ^{14}C around 1985 and remains above tropospheric Δ^{14}C thereafter. The

621   global average Δ^{14}C of vegetation declined from -5.4 to -18.7‰ from 1850 to 1955, increased in

622   the next 25 years to peak around +180‰ and declined by about 50‰ until 2010. The global-

623   average bomb Δ^{14}C signals in soil carbon, including coarse woody debris and litter, is

624   substantially smaller than in vegetation carbon and peak Δ^{14}C is further delayed. Δ^{14}C in soil

625   carbon increased from around -137‰ to -102‰ from 1955 to 1990. These responses in Δ^{14}C are

626   consistent with an increase in mean age (Bolin and Rodhe, 1973) from heterotrophic respiration,

627   to vegetation carbon, and to soil carbon.

628   **3.4 The preindustrial distribution of Δ^{14}C in the ocean**

629   The comparison of observed versus simulated Δ^{14}C(DIC) in the surface ocean (Fig. 6 and 7)

630   suggests that the air-sea gradient of Δ^{14}C is represented roughly in agreement with observational

631   estimates. The global mean area-weighted surface ocean Δ^{14}C is 1.5‰ lower in the model

632   (SPIN_OC; -67.94 ‰) than in the GLODAP data (-66.47 ‰). The root mean square deviation

633   between model and GLODAP data is 9‰. Surface Δ^{14}C is overestimated in parts of the Pacific

634   and Indian sectors of the Southern Ocean and underestimated in the Atlantic sector (Fig. 7).

635   Surface Δ^{14}C is also underestimated in the northern North Atlantic and Pacific (Fig. 7).

636

637   **Figure 6:** Simulated (black dash) versus observation-based (black solid) (Key et al., 2004) basin-mean Δ^{14}C(DIC)

638   profiles for the preindustrial period. The blue lines show the preindustrial model results for the abiotic radiocarbon

639   tracer. The radiocarbon tracers still show some drift at the end of the spin-up which affects the simulated differences

640   between these two tracers. The Southern Ocean includes the area south of 35°S and these areas are not included in

641   the profiles for the Atlantic, Pacific, and Indian Ocean. The model is only sampled where GLODAP gridded data are

642   available; the Arctic Ocean and some other smaller oceans are not covered by the GLODAP data.
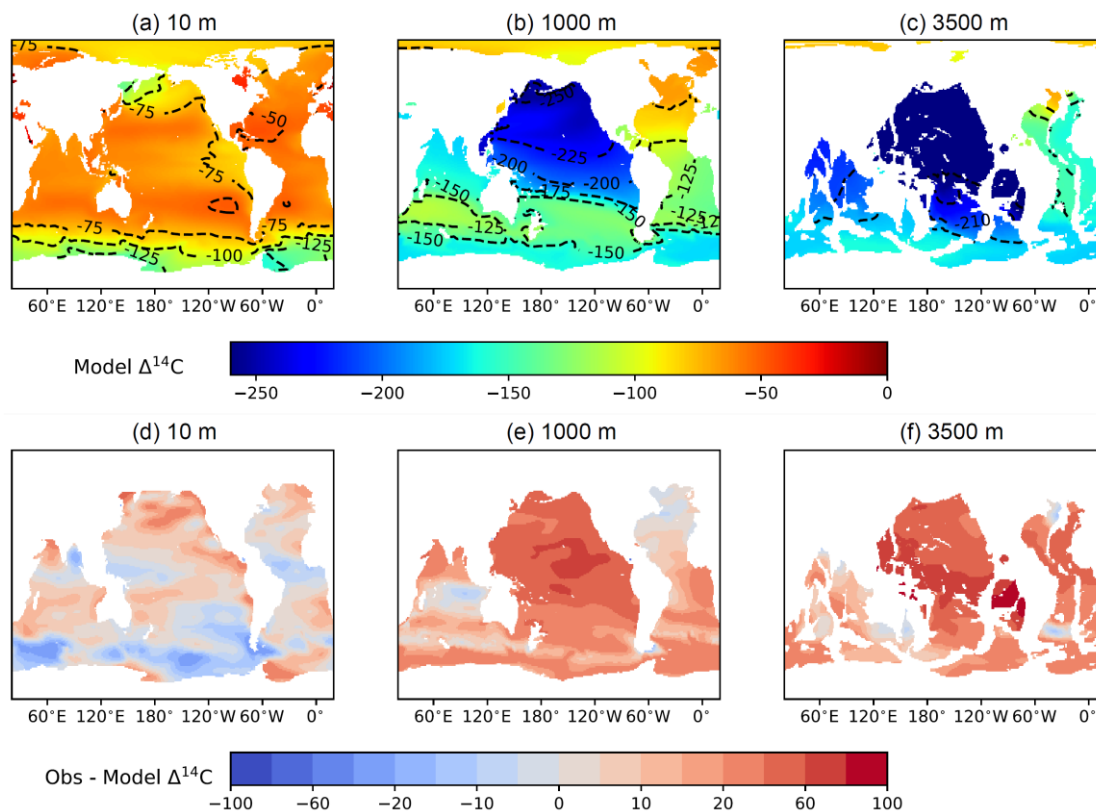
643

644   In contrast to the surface, Δ^{14}C(DIC) is consistently underestimated in the deep ocean by POP2

645   (Fig. 6, 7). Below the surface, radioactive decay of ^{14}C acts as a sink process, and Δ^{14}C decreases

646   along the flow path of a water mass. Basin-average differences between model and observational

647   data are about 5‰ in the upper Atlantic and grow to about 45‰ in the deepest waters. This

648   implies that the radiocarbon age of the deep Atlantic is overestimated by about 450 years. Even

649   larger mean biases of around 70‰, or 770 years in age, are found at around 2000 m in the

650   Pacific, while mean biases are smaller and less than ~25‰ (250 years) in the Indian and Southern

651   Ocean. Ocean overturning and ventilation of the deep water masses are too sluggish in the POP2

652   model. This is a known model bias of POP2 as discussed by Jahn et al. (2015, and references

653   therein)

654   **3.5 Abiotic versus biotic ^{14}C tracers**

655   Next, results for the abiotic versus biotic ^{14}C formulations are compared to test the validity of the

656   simpler and less computing demanding abiotic formulation. We recall from the method section

657   that fluxes between DIC and organic matter are neglected for the calculation of the abiotic tracer.

658   The basin-mean profiles in the upper thermocline and the entire Atlantic show close agreement

659   between abiotic and biotic Δ^{14}C (blue vs dashed line in Fig. 6). Mean Δ^{14}C differences in the

660   Southern Ocean are relatively small, while substantial differences are simulated in the Indian, and

661   in particular in the deep Pacific. Δ^{14}C in the biotic simulation is consistently less negative

662   (younger) than in the abiotic simulations at depth. This may be expected as the remineralization

663   of organic material adds DIC with a relatively high Δ^{14}C to the deep DIC pool. However, model

664   drift in the deep ocean affects this comparison between the abiotic and biotic tracer at the end of

665   the spin-up and calls for caution.

666   The good agreement in biotic and abiotic Δ^{14}C in the upper ocean and the Atlantic, as well as

667   higher biotic than abiotic Δ^{14}C (Fig. 6), is in contrast to the findings of Jahn et al. (2015). These

668   authors show biotic Δ^{14}C to be around 40‰ lower than abiotic Δ^{14}C at the surface and for 1990

669   CE (their Fig. 4). Biotic Δ^{14}C is also lower than abiotic Δ^{14}C throughout the water column and

670   therefore in waters not affected by the bomb signal. It appears that the large difference between

671   biotic and abiotic Δ^{14}C presented by Jahn et al. is explained by their atmospheric boundary

672   condition for the biotic tracer. Too low biotic Δ^{14}C values are simulated when inadvertently

673   prescribing atmospheric Δ^{14}C instead of atmospheric δ^{14}C to the biotic ^{14}C tracer. The difference

674   between δ^{14}C and Δ^{14}C amounts to about 37‰ $(2*(\delta^{13}C+25))$ for a preindustrial δ^{13}C of -

675   6.379‰ as used by Jahn et al. (2015).

Figure 7: Simulated versus observation-based distribution of Δ^{14}C(DIC) for the preindustrial period at the surface, 1000 m, and at 3500 m. Model results (top panels) are from the end of the spin-up simulation SPIN_OC. The lower panels show the difference of observation-based Δ^{14}C (Key et al., 2004) minus simulated Δ^{14}C.

4 Discussion

The Earth system budget of "excess" or "bomb" ^{14}C is revisited in this study. The purpose is to evaluate the cycling of ^{14}C and underlying carbon cycle and physical and biological processes in the land (CLM5) and ocean (POP2) components of the Community Earth System Model (CESM2). We performed simulations with POP2 and CLM5 in stand-alone mode and forced with prescribed atmospheric CO_2 and $^{14}CO_2$ under preindustrial conditions and over the historical period. In addition to the standard Normal Year Forcing (NYF) of Large and Yeager (2009), we also performed a historical period simulation using the Japanese Reanalysis Data (JRA55), which implies different winds and therefore different air-sea gas exchange piston velocities and bomb ^{14}C transfer than under NYF. Imbalances in the Earth system budget of bomb ^{14}C are diagnosed by comparing the cumulative bomb ^{14}C production from bomb-test statistics and the observation-based stratospheric and tropospheric and modeled ocean and terrestrial bomb ^{14}C inventories.

4.1 A low bias in the simulated uptake of bomb ^{14}C by trees indicates biases in carbon allocation and overturning time scales in CLM5

Imbalances in the Earth system bomb ^{14}C budget accumulate mainly in the 1960s, while the production records and inventory changes are consistent after 1970 (Fig. 1, black versus magenta lines). These imbalances suggest a too-low simulated uptake of ^{14}C from the atmosphere during the 1960s. The bomb ^{14}C inventory simulated by POP2 under NYF for the GEOSCES and WOCE era is well within the range of central observation-based estimates from a range of studies (Fig.1 solid blue curve and symbols). In contrast, the inventory of bomb ^{14}C in CLM5 remains below the lower uncertainty bound of the observational estimate of Naegler and Levin (2009a) for the period 1963 to 1990 (Fig. 5b). Naegler and Levin considered uncertainties in ocean uptake, the stratospheric and tropospheric inventory, and the production rates of bomb ^{14}C to derive their uncertainty bound for the land biosphere inventory. This estimate and the Earth system budget of bomb ^{14}C both rely on the same bomb ^{14}C production records and atmospheric inventory data and therefore share some common uncertainties. The results suggest that CLM5 simulates a too-low uptake of bomb ^{14}C, mainly in the 1960s, and that this low uptake explains, at least partly, the imbalances in the Earth system budget and the deviation between simulated and observation-derived land biosphere inventory of bomb [14]C.

The combined inventory of bomb ^{14}C in the atmosphere and modeled by POP2 and CLM5 declined by about 10% from 1964 to 1967 in the absence of any relevant other sinks (Fig. 1, magenta). This implies that either the observation-inferred decline in the stratospheric and tropospheric inventories is too larger and/or modeled ocean and land uptakes are too low. This decline is too large to be explained by uncertainties of a single factor, but can likely only be removed by a downward revision of the atmospheric inventory decline in combination with an upward revision of CLM5, and, perhaps, POP2 bomb ^{14}C uptake.

CLM5 underestimates the net carbon sink on land during the period 1945 to 1970 and this translates into a deficit in ^{14}C uptake of about 2 kmol. Thus, a better representation of the net carbon sink in CLM5 would potentially tend to narrow the gap between the modeled and observation-based bomb ^{14}C inventory of the land biosphere.

720   The CLM5 results show that forests are the largest sink of bomb ^{14}C in the land biosphere (Fig.

721   2). This carbon reservoir is of high importance for the land sink of anthropogenic carbon (Arora

722   et al., 2020). We argue that too low bomb ^{14}C sequestration by wood in CLM5 is mainly

723   responsible for the low bias of the simulated global land biosphere bomb ^{14}C inventory. Grasses

724   and shrub ecosystems have a small above-ground carbon inventory. In turn, the vegetation of

725   these systems cannot sequester much bomb ^{14}C. Similarly, the short-turnover time and the low

726   carbon inventory of leaves and needles and fine roots do restrict their potential for bomb ^{14}C

727   sequestration. Soils could potentially sequester a lot of bomb ^{14}C given their large carbon stocks

728   and slow overturning. However, Δ^{14}C in modern soils is consistently overestimated in CLM5

729   (Shi et al., 2020), suggesting rather a too large and not a too low uptake of bomb ^{14}C by soils in

730   CLM5. Taken together, we conclude that the uptake of ^{14}C by forest vegetation and stem and

731   branches is biased low. In turn, the carbon fluxes allocated to wood and/or the overturning time

732   scales of wood carbon in forests are probably biased low in CLM5. This could potentially also be

733   associated with a low bias in NPP of forest ecosystems

734   **4.2 Biotic and abiotic ^{14}C in the POP2 ocean: a too slow deep ocean circulation**

735   The POP2 ocean model simulates the highest bomb ^{14}C column inventories in the well-ventilated

736   water masses of the North Atlantic and Antarctic Intermediate and Mode waters. The modeled

737   penetration of bomb Δ^{14}C compares reasonably well with the gridded GLODAP data suggesting

738   that ventilation time scales are reasonable for the global thermocline in agreement with earlier

739   findings (Danabasoglu et al., 2009). A more thorough comparison of ocean model results with

740   station data and along repeat sections is beyond the scope of this study.

741   The increase in Δ^{14}C over the bomb test period as recorded by corals and bivalves in the North

742   Atlantic and the low latitude Indian and Pacific oceans is generally underestimated by POP2. It is

743   unclear whether a too low piston velocity, a too rapid surface-to-deep transfer at these proxy

744   locations, or a sampling bias is the cause of this mismatch and further studies are needed to

745   clarify this.

746   Preindustrial, natural Δ^{14}C is biased low in particular in the deep ocean with the largest basin-

747   mean age biases of order 450 years below 3000 m in the Atlantic and 770 years at 2000 m in the

748   Pacific, similar to the results obtained by Jahn et al. (2015) with a lower resolution version of

749   POP2. This points to a too slow overturning circulation of the deep ocean in POP2. This large

750   bias in deep ocean ventilation likely affects projections of atmospheric CO_2 and global warming,

751   ocean heat uptake and sea-level rise, and ocean acidification and deoxygenation.

752   POP2 includes two radiocarbon tracers. For the biotic tracer, ^{14}C fluxes related to the marine

753   biological cycle and fractionation are considered, whereas these processes are neglected for the

754   abiotic tracer. We find close agreement between simulated biotic and abiotic $\Delta^{14}C$ in the upper

755   ocean at preindustrial after accounting for differences in the implementation of atmospheric

756   boundary conditions in POP2. This confirms that results from the simpler, abiotic $\Delta^{14}C$ tracer are

757   useful to evaluate ocean ventilation time scales. Larger deviations are simulated in the deep Indo-

758   Pacific, with less negative $\Delta^{14}C$ values for the biotic than abiotic tracer. It is not clear whether

759   these deviations are due to the addition of ^{14}C rich carbon by organic matter remineralization to

760   the biotic ^{14}C tracer or due to model drift at these deep locations.

761   **4.3 Implications for the air-sea gas transfer piston velocity**

762   The magnitude of the piston velocity is key to correctly simulate the ocean uptake of bomb ^{14}C.

763   In this study, the piston velocity is computed using a quadratic wind speed relationship (Eq. 2)

764   and the value (0.251 cm h^{-1} m^{-2} s^{-2}) of the scaling factor a by Wanninkhof (2014) in combination

765   with the NYF of Large and Yeager (2009) for the spin-up and the historical period and with the

766   JRA55 wind product for a sensitivity simulation over the historical period. The observation-based

767   bomb ^{14}C inventories at the time of the GEOSECS and WOCE surveys are well-matched by the

768   POP2 simulation with NYF, lending support to use the NYF wind data together with the scaling

769   of Wanninkhof (2014). Jahn et al. (2015) applied a 24% larger coefficient (0.31 cm h^{-1} m^{-2} s^{-2})

770   than used here. Correspondingly, the simulated bomb ^{14}C inventory is at the upper end of the

771   observational range (Fig. 1, black x versus blue symbol with error bar).

772   The modeled ocean inventories are in the lower observational range for JRA55 and Earth system

773   ^{14}C budget imbalances become larger when applying the JRA55 instead of NYF wind data. The

774   low global ocean bomb inventories and large budget imbalances suggest that a larger value of a

775   should be applied than used here for the JRA55 product to simulate ocean bomb ^{14}C uptake. We

776   estimate a correction to a for use with JRA55 winds as follows. An upward correction of 4.4

777   kmol is required to bring the bomb ^{14}C inventories simulated with JRA55 to agree with the

778 central bomb ^{14}C inventory estimate of 40.1 kmol for 1975 and of 56.7 kmol for 1995 from

779 Naegler and Levin (2006). This would also reduce the Earth system budget imbalance after 1970

780 (Fig. 1, magenta dashed curve) by the same amount. We apply the sensitivities, i.e., the relative

781 change in inventory simulated by the Bern3D model to the relative change in piston velocity

782 (Müller et al. (2008); their Tab. 3). An increase of 16.5% and 14.3% in a is required to increase

783 the ocean bomb ^{14}C inventory by 4.4 kmol at 1975 and 1995. This yields an estimate for a of

784 about 2.9 cm h^{-1} m^{-2} s^{-2}. This correction is within the overall uncertainty range for the piston

785 velocity of 20% given by Wanninkhof (2014) but larger than the uncertainty of 5% to 10%

786 suggested by Woolf et al. (2019). Iida et al. (2020) adjusted the scaling factor a of Eq. 2 for the

787 JRA55 wind fields by 3% from 0.251 to 0.259 based on a comparison of the Cross Calibrated

788 Multi-Platform (CCMP) wind product used by Wanninkhof (2014) and JRA55 winds. The

789 correction proposed here is larger, possibly because spatio-temporal variations in the air-sea

790 $^{14}CO_2$ gradient and air-sea ^{14}C fluxes are explicitly considered in the POP2 simulation.

791 The correction affects the estimates of the net air-to-sea tracer fluxes derived from observations

792 of the atmosphere-surface ocean partial pressure (or fugacity) differences. The recent global air-

793 sea CO_2 flux estimate of 2±0.5 GtC yr^{-1} for the period from 1993 to 2008 by Iida et al. (2020) is

794 12% higher when accounting for the higher value of a as estimated in this study. This correction

795 brings the central estimate of the average air-sea flux by Iida et al. closer to the estimate of

796 Gruber et al (2019) for the annual mean change in ocean carbon inventory (2.4±0.3 PgC yr^{-1}) as

797 derived from ocean interior data and for 1994 to 2008.

798 Watson et al. (2020) calculated air-sea CO_2 fluxes globally from the Surface Ocean Carbon

799 Dioxide Atlas (SOCAT) and corrected for temperature differences between the depth of CO_2

800 sampling and the ocean surface and assuming a fixed temperature and salinity gradients across

801 the ocean skin (~100 μm). Such corrections are implicitly accounted for when the piston velocity

802 is scaled to bring modeled and observation-derived ocean bomb ^{14}C inventories to agree.

803 Interestingly, ocean-mean wind speed and piston velocity are higher for the JRA55 than the NYF

804 data, despite that bomb ^{14}C inventories are lower under JRA55 forcing. This is in contrast to the

805 expectation that a higher ocean-mean piston velocity yields also higher bomb inventories,

806 pointing to the potential importance of spatio-temporal patterns. The global mean squared wind

807 speed over the ocean is 8% higher for JRA55 (1958 to 1977: 67.65 m^2 s^{-2}; range of annual values:

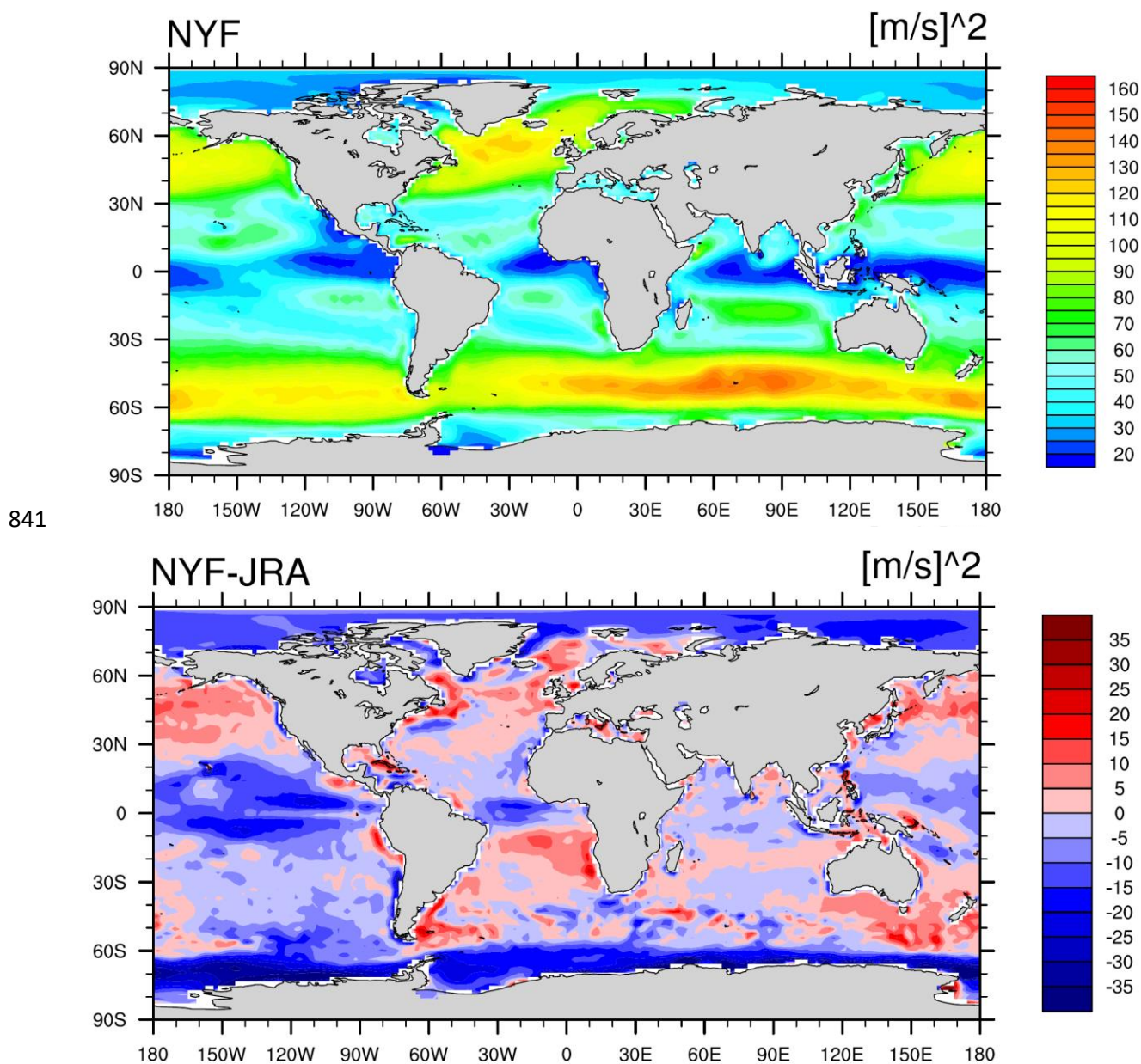808   66.69 to 68.78 m^2 s^{-2}) than NYF (62.70 m^2 s^{-2}). Wind speeds of JRA55 are higher than of NYF in

809   particular over ice-covered areas of the Arctic and the Southern Ocean, but also over large parts

810   of the low latitude ocean and the southern Pacific (Appendix Fig. A.1). On the other hand, wind

811   speeds of NYF are generally higher in mid-latitude areas. The global mean piston velocity

812   normalized to a Schmidt number of 660 is 16.2 cm h^{-1} for NYF and 17.5 cm h^{-1} for the JRA55

813   product after applying the 3% upward correction for the ice-free ocean suggested by Naegler

814   (2009). These values are lower but within the range of Naegler (2009) who proposes a global

815   mean normalized piston velocity of 18.2±3.6 cm h^{-1} over the ice-free ocean by summarizing

816   estimates from four different studies (Müller et al., 2008;Sweeney et al., 2007;Krakauer et al.,

817   2006;Naegler et al., 2006). Specifically, the piston velocities from NYF, yielding a match of

818   simulated bomb inventories with observational estimates, are on a global average 11% lower than

819   the central estimate of Naegler (2009). This finding suggests that the overall uncertainty in the

820   piston velocity is larger than 10% and lower uncertainty ranges for the piston velocity may be too

821   optimistic. The POP2 results show that differences in the spatio-temporal patterns of wind speed

822   and, hence, of the piston velocity are, in addition to differences in global mean values, important

823   and influence modeled global bomb ^{14}C inventories.

824   **5. Conclusions**

825   The analysis of bomb- and naturally-produced ^{14}C provides insight into the timescales and

826   processes governing the global carbon cycle, atmospheric CO_2, and climate. Our results suggest

827   that the carbon flux allocated to wood and/or the overturning time scales of wood carbon in

828   forests are biased low in the land biosphere model CLM5 and that the deep ocean ventilation is

829   too slow in the POP2 ocean model. Modeled global ocean bomb ^{14}C inventories are consistent

830   with observational estimates for the air-sea gas exchange piston velocity parameterization of

831   Wanninkhof (2014) combined with NYF wind data. In contrast, the simulated ocean inventories

832   are low when using the JRA55 instead NYF winds and we suggest an upward revision of the

833   parameterization by 15% for the JRA55 product. Future efforts may be directed to adapt CLM5

834   and POP2 formulations to lower the identified biases in CLM5 and POP2. Another task is to

835   simulate ^{14}C in fully coupled Earth system models with natural (Masarik and Beer,

836   2009;Kovaltsov et al., 2012) and anthropogenic ^{14}C sources prescribed in the atmosphere. This

837   may enable further testing of transport time scales of Earth system models used for future

838   projections of atmospheric CO_2 and climate.

839

840   **Appendix A: Wind speed**

841

842

843   Fig. A1: Annual mean of the wind speed squared at 10 m as used to compute the air-sea gas

844   exchange piston velocity for (top) the Normal Year Forcing (NYF) and (bottom) the difference

845   between NYF minus Japanese Reanalysis (JRA55) wind data. JRA55 winds are averaged over

846   the period from 1958 to 1977; NYF data cover one year.

847

Acknowledgements and Data

The model code for CESM2 is publicly available: https://www.cesm.ucar.edu/models/cesm2/release_download.html. ^{14}C records are available on the NOAA data server: https://www1.ncdc.noaa.gov/pub/data/paleo/archive/ . The data used to produce the figures will be made available on a repository.

FJ wrote the paper and designed the study with input from all authors and based on the master thesis of TF. TF and AE carried out the simulations. TF prepared the figures.

References

Arora, V. K., Katavouta, A., Williams, R. G., Jones, C. D., Brovkin, V., Friedlingstein, P., Schwinger, J., Bopp, L., Boucher, O., Cadule, P., Chamberlain, M. A., Christian, J. R., Delire, C., Fisher, R. A., Hajima, T., Ilyina, T., Joetzjer, E., Kawamiya, M., Koven, C. D., Krasting, J. P., Law, R. M., Lawrence, D. M., Lenton, A., Lindsay, K., Pongratz, J., Raddatz, T., Séférian, R., Tachiiri, K., Tjiputra, J. F., Wiltshire, A., Wu, T., and Ziehn, T.: Carbon–concentration and carbon–climate feedbacks in CMIP6 models and their comparison to CMIP5 models, Biogeosciences, 17, 4173-4222, 10.5194/bg-17-4173-2020, 2020.

Bé, M.-M., Chisté, V., Dulieu, C., Mougeot, X., Chechev, V. P., Kondev, F. G., Nichols, A. L., Huang, X., and Wang, B.: Table of Radionuclides, volume 7 of Monographie BIPM-5, Bureau International des Poids et Mesures, Pavillon de Breteuil, F-92310 Sèvres, France, 2013.

Bolin, B., and Rodhe, H.: A note on the concepts of age distribution and transit time in natural reservoirs, Tellus, 25, 58-62, 10.1111/j.2153-3490.1973.tb01594.x, 1973.

Braziunas, T. F., Fung, I. Y., and Stuiver, M.: The preindustrial atmospheric14CO2 latitudinal gradient as related to exchanges among atmospheric, oceanic, and terrestrial reservoirs, Global Biogeochemical Cycles, 9, 565-584, 10.1029/95gb01725, 1995.

883 Broecker, W. S., Peng, T.-H., Ostlund, G., and Stuiver, M.: The distribution of bomb radiocarbon in the
884 ocean, Journal of Geophysical Research: Oceans, 90, 6953-6970, 10.1029/JC090iC04p06953, 1985.
885 Broecker, W. S., Sutherland, S., Smethie, W., Peng, T.-H., and Ostlund, G.: Oceanic radiocarbon:
886 Separation of the natural and bomb components, Global Biogeochemical Cycles, 9, 263-288,
887 10.1029/95GB00208, 1995.
888 Danabasoglu, G., Peacock, S., Lindsay, K., and Tsumune, D.: Sensitivity of CFC-11 uptake to physical initial
889 conditions and interannually varying surface forcing in a global ocean model, Ocean Modelling, 29, 58-
890 65, https://doi.org/10.1016/j.ocemod.2009.02.011, 2009.
891 Danabasoglu, G., Bates, S. C., Briegleb, B. P., Jayne, S. R., Jochum, M., Large, W. G., Peacock, S., and
892 Yeager, S. G.: The CCSM4 Ocean Component, Journal of Climate, 25, 1361-1389, 10.1175/JCLI-D-11-
893 00091.1, 2012.
894 Danabasoglu, G., Lamarque, J. F., Bacmeister, J., Bailey, D. A., DuVivier, A. K., Edwards, J., Emmons, L. K.,
895 Fasullo, J., Garcia, R., Gettelman, A., Hannay, C., Holland, M. M., Large, W. G., Lauritzen, P. H., Lawrence,
896 D. M., Lenaerts, J. T. M., Lindsay, K., Lipscomb, W. H., Mills, M. J., Neale, R., Oleson, K. W., Otto-Bliesner,
897 B., Phillips, A. S., Sacks, W., Tilmes, S., van Kampenhout, L., Vertenstein, M., Bertini, A., Dennis, J., Deser,
898 C., Fischer, C., Fox-Kemper, B., Kay, J. E., Kinnison, D., Kushner, P. J., Larson, V. E., Long, M. C., Mickelson,
899 S., Moore, J. K., Nienhouse, E., Polvani, L., Rasch, P. J., and Strand, W. G.: The Community Earth System
900 Model Version 2 (CESM2), Journal of Advances in Modeling Earth Systems, 12, e2019MS001916,
901 10.1029/2019MS001916, 2020.
902 Dentith, J. E., Ivanovic, R. F., Gregoire, L. J., Tindall, J. C., Robinson, L. F., and Valdes, P. J.: Simulating
903 oceanic radiocarbon with the FAMOUS GCM: implications for its use as a proxy for ventilation and
904 carbon uptake, Biogeosciences Discuss., 2019, 1-46, 10.5194/bg-2019-365, 2019.
905 Dirmeyer, P. A., Gao, X., Zhao, M., Guo, Z., Oki, T., and Hanasaki, N.: GSWP-2: Multimodel Analysis and
906 Implications for Our Perception of the Land Surface, Bulletin of the American Meteorological Society, 87,
907 1381-1398, 10.1175/BAMS-87-10-1381, 2006.
908 Druffel, E. R. M.: Radiocarbon in Corals: Records of the Carbon Cycle, Surface Circulation and Climate,
909 Oceanography, 15, 10.5670/oceanog.2002.43, 2002.
910 Eide, M., Olsen, A., Ninnemann, U. S., and Johannessen, T.: A global ocean climatology of preindustrial
911 and modern ocean δ13C, Global Biogeochemical Cycles, n/a-n/a, 10.1002/2016gb005473, 2017.
912 Enting, I.: Nuclear weapons data for use in carbon cycle modelling, CSIRO Div. of Atmos. Res.,
913 Melbourne, Australia, 1982.
914 Eyring, V., Bony, S., Meehl, G. A., Senior, C. A., Stevens, B., Stouffer, R. J., and Taylor, K. E.: Overview of
915 the Coupled Model Intercomparison Project Phase 6 (CMIP6) experimental design and organization,
916 Geosci. Model Dev., 9, 1937-1958, 10.5194/gmd-9-1937-2016, 2016.
917 Fallon, S. J., and Guilderson, T. P.: Surface water processes in the Indonesian throughflow as documented
918 by a high-resolution coral Δ14C record, Journal of Geophysical Research: Oceans, 113,
919 https://doi.org/10.1029/2008JC004722, 2008.
920 Farquhar, G. D., Ehleringer, J. R., and Hubick, K. T.: Carbon isotope discrimination and photosynthesis,
921 Annu. Rev. Plant Physiol, 40, 503-537, 1989.
922 Friedlingstein, P., Jones, M. W., O'Sullivan, M., Andrew, R. M., Hauck, J., Peters, G. P., Peters, W.,
923 Pongratz, J., Sitch, S., Le Quéré, C., Bakker, D. C. E., Canadell, J. G., Ciais, P., Jackson, R. B., Anthoni, P.,
924 Barbero, L., Bastos, A., Bastrikov, V., Becker, M., Bopp, L., Buitenhuis, E., Chandra, N., Chevallier, F., Chini,
925 L. P., Currie, K. I., Feely, R. A., Gehlen, M., Gilfillan, D., Gkritzalis, T., Goll, D. S., Gruber, N., Gutekunst, S.,
926 Harris, I., Haverd, V., Houghton, R. A., Hurtt, G., Ilyina, T., Jain, A. K., Joetzjer, E., Kaplan, J. O., Kato, E.,
927 Klein Goldewijk, K., Korsbakken, J. I., Landschützer, P., Lauvset, S. K., Lefèvre, N., Lenton, A., Lienert, S.,
928 Lombardozzi, D., Marland, G., McGuire, P. C., Melton, J. R., Metzl, N., Munro, D. R., Nabel, J. E. M. S.,
929 Nakaoka, S. I., Neill, C., Omar, A. M., Ono, T., Peregon, A., Pierrot, D., Poulter, B., Rehder, G., Resplandy,
930 L., Robertson, E., Rödenbeck, C., Séférian, R., Schwinger, J., Smith, N., Tans, P. P., Tian, H., Tilbrook, B.,

931   Tubiello, F. N., van der Werf, G. R., Wiltshire, A. J., and Zaehle, S.: Global Carbon Budget 2019, Earth Syst.
932   Sci. Data, 11, 1783-1838, 10.5194/essd-11-1783-2019, 2019.
933   Graven, H., Allison, C. E., Etheridge, D. M., Hammer, S., Keeling, R. F., Levin, I., Meijer, H. A. J., Rubino, M.,
934   Tans, P. P., Trudinger, C. M., Vaughn, B. H., and White, J. W. C.: Compiled records of carbon isotopes in
935   atmospheric CO2 for historical simulations in CMIP6, Geosci. Model Dev., 10, 4405-4417, 10.5194/gmd-
936   10-4405-2017, 2017.
937   Graven, H. D., and Gruber, N.: Continental-scale enrichment of atmospheric
938   ^{14}CO$_2$ from the nuclear power industry: potential impact on the estimation of
939   fossil fuel-derived CO$_2$, Atmos. Chem. Phys., 11, 12339-12349, 10.5194/acp-11-12339-2011,
940   2011.
941   Graven, H. D.: Impact of fossil fuel emissions on atmospheric radiocarbon and various applications of
942   radiocarbon over this century, Proceedings of the National Academy of Sciences, 112, 9542,
943   10.1073/pnas.1504467112, 2015.
944   Grottoli, A. G., and Eakin, C. M.: A review of modern coral δ18O and Δ14C proxy records, Earth-Science
945   Reviews, 81, 67-91, https://doi.org/10.1016/j.earscirev.2006.10.001, 2007.
946   Gruber, N., Clement, D., Carter, B. R., Feely, R. A., van Heuven, S., Hoppema, M., Ishii, M., Key, R. M.,
947   Kozyr, A., Lauvset, S. K., Lo Monaco, C., Mathis, J. T., Murata, A., Olsen, A., Perez, F. F., Sabine, C. L.,
948   Tanhua, T., and Wanninkhof, R.: The oceanic sink for anthropogenic CO$_2$ from
949   1994 to 2007, Science, 363, 1193, 10.1126/science.aau5153, 2019.
950   Grumet, N., Guilderson, T. P., and Dunbar, R. B.: PRE-BOMB RADIOCARBON VARIABILITY INFERRED FROM
951   A KENYAN CORAL RECORD, Radiocarbon, 44, 581-590, 2002.
952   Guilderson, T. P., Schrag, D. P., Goddard, E., Kashgarian, M., Wellington, G. M., and Linsley, B. K.:
953   Southwest Subtropical Pacific Surface Water Radiocarbon in a High-Resolution Coral Record,
954   Radiocarbon, 42, 249-256, 10.1017/S0033822200059051, 2000.
955   Guilderson, T. P., Schrag, D. P., and Cane, M. A.: Surface Water Mixing in the Solomon Sea as
956   Documented by a High-Resolution Coral 14C Record, Journal of Climate, 17, 1147-1156, 10.1175/1520-
957   0442(2004)017<1147:SWMITS>2.0.CO;2, 2004.
958   Guilderson, T. P., Fallon, S., Moore, M. D., Schrag, D. P., and Charles, C. D.: Seasonally resolved surface
959   water Δ14C variability in the Lombok Strait: A coralline perspective, Journal of Geophysical Research:
960   Oceans, 114, https://doi.org/10.1029/2008JC004876, 2009.
961   He, Y., Trumbore, S. E., Torn, M. S., Harden, J. W., Vaughn, L. J. S., Allison, S. D., and Randerson, J. T.:
962   Radiocarbon constraints imply reduced carbon uptake by soils during the 21st century, Science, 353,
963   1419, 2016.
964   Hesshaimer, V., Heimann, M., and Levin, I.: Radiocarbon evidence for a smaller oceanic carbon dioxide
965   sink than previously believed, Nature, 370, 201-203, 1994.
966   Hogg, A. G., Heaton, T. J., Hua, Q., Palmer, J. G., Turney, C. S. M., Southon, J., Bayliss, A., Blackwell, P. G.,
967   Boswijk, G., Bronk Ramsey, C., Pearson, C., Petchey, F., Reimer, P., Reimer, R., and Wacker, L.: SHCal20
968   Southern Hemisphere Calibration, 0–55,000 Years cal BP, Radiocarbon, 62, 759-778,
969   10.1017/RDC.2020.59, 2020.
970   Hurrell, J. W., Holland, M. M., Gent, P. R., Ghan, S., Kay, J. E., Kushner, P. J., Lamarque, J. F., Large, W. G.,
971   Lawrence, D., Lindsay, K., Lipscomb, W. H., Long, M. C., Mahowald, N., Marsh, D. R., Neale, R. B., Rasch,
972   P., Vavrus, S., Vertenstein, M., Bader, D., Collins, W. D., Hack, J. J., Kiehl, J., and Marshall, S.: The
973   Community Earth System Model: A Framework for Collaborative Research, Bulletin of the American
974   Meteorological Society, 94, 1339-1360, 10.1175/bams-d-12-00121.1, 2013.
975   Hurtt, G. C., Chini, L., Sahajpal, R., Frolking, S., Bodirsky, B. L., Calvin, K., Doelman, J. C., Fisk, J., Fujimori,
976   S., Klein Goldewijk, K., Hasegawa, T., Havlik, P., Heinimann, A., Humpenöder, F., Jungclaus, J., Kaplan, J.
977   O., Kennedy, J., Krisztin, T., Lawrence, D., Lawrence, P., Ma, L., Mertz, O., Pongratz, J., Popp, A., Poulter,
978   B., Riahi, K., Shevliakova, E., Stehfest, E., Thornton, P., Tubiello, F. N., van Vuuren, D. P., and Zhang, X.:

979   Harmonization of global land use change and management for the period 850–2100 (LUH2) for CMIP6,
980   Geosci. Model Dev., 13, 5425-5464, 10.5194/gmd-13-5425-2020, 2020.
981   Iida, Y., Takatani, Y., Kojima, A., and Ishii, M.: Global trends of ocean CO2 sink and ocean acidification: an
982   observation-based reconstruction of surface ocean inorganic carbon variables, Journal of Oceanography,
983   10.1007/s10872-020-00571-5, 2020.
984   Jahn, A., Lindsay, K., Giraud, X., Gruber, N., Otto-Bliesner, B. L., Liu, Z., and Brady, E. C.: Carbon isotopes
985   in the ocean model of the Community Earth System Model (CESM1), Geoscientific Model Development,
986   8, 2419-2434, 2015.
987   Joos, F.: Bomb Radiocarbon - Imbalance in the Budget, Nature, 370, 181-182, 1994.
988   Joos, F., Meyer, R., Bruno, M., and Leuenberger, M.: The variability in the carbon sinks as reconstructed
989   for the last 1000 years, Geophysical Research Letters, 26, 1437-1440, 1999.
990   Keller, K. M., Lienert, S., Bozbiyik, A., Stocker, T. F., Churakova, O. V., Frank, D. C., Klesse, S., Koven, C. D.,
991   Leuenberger, M., Riley, W. J., Saurer, M., Siegwolf, R., Weigt, R. B., and Joos, F.: 20th century changes in
992   carbon isotopes and water-use efficiency: tree-ring-based evaluation of the CLM4.5 and LPX-Bern
993   models, Biogeosciences, 14, 2641-2673, 10.5194/bg-14-2641-2017, 2017.
994   Kennedy, D., Swenson, S., Oleson, K. W., Lawrence, D. M., Fisher, R., Lola da Costa, A. C., and Gentine, P.:
995   Implementing Plant Hydraulics in the Community Land Model, Version 5, Journal of Advances in
996   Modeling Earth Systems, 11, 485-513, 10.1029/2018MS001500, 2019.
997   Key, R. M., Kozyr, A., Sabine, C. L., Lee, K., Wanninkhof, R., Bullister, J. L., Feely, R. A., Millero, F. J.,
998   Mordy, C., and Peng, T. H.: A global ocean carbon climatology: Results from Global Data Analysis Project
999   (GLODAP), Global Biogeochem. Cycles, 18, GB4031, 10.1029/2004GB002247, 2004.
1000   Khatiwala, S., Primeau, F., and Holzer, M.: Ventilation of the deep ocean constrained with tracer
1001   observations and implications for radiocarbon estimates of ideal mean age, Earth and Planetary Science
1002   Letters, 325-326, 116-125, https://doi.org/10.1016/j.epsl.2012.01.038, 2012.
1003   Kilbourne, K. H., Quinn, T. M., Guilderson, T. P., Webb, R. S., and Taylor, F. W.: Decadal- to interannual-
1004   scale source water variations in the Caribbean Sea recorded by Puerto Rican coral radiocarbon, Climate
1005   Dynamics, 29, 51-62, 10.1007/s00382-007-0224-2, 2007.
1006   Kobayashi, S., Ota, Y., Harada, Y., Ebita, A., Moriya, M., Onoda, H., Onogi, K., Kamahori, H., Kobayashi, C.,
1007   Endo, H., Miyaoka, K., and Takahashi, K.: The JRA-55 Reanalysis: General Specifications and Basic
1008   Characteristics, Journal of the Meteorological Society of Japan. Ser. II, 93, 5-48, 10.2151/jmsj.2015-001,
1009   2015.
1010   Kovaltsov, G. A., Mishev, A., and Usoskin, I. G.: A new model of cosmogenic production of radiocarbon
1011   14C in the atmosphere, Earth and Planetary Science Letters, 337–338, 114-120,
1012   10.1016/j.epsl.2012.05.036, 2012.
1013   Koven, C. D., Riley, W. J., Subin, Z. M., Tang, J. Y., Torn, M. S., Collins, W. D., Bonan, G. B., Lawrence, D.
1014   M., and Swenson, S. C.: The effect of vertically resolved soil biogeochemistry and alternate soil C and N
1015   models on C dynamics of CLM4, Biogeosciences, 10, 7109-7131, 10.5194/bg-10-7109-2013, 2013.
1016   Krakauer, N. Y., Randerson, J. T., Primeau, F. W., Gruber, N., and Menemenlis, D.: Carbon isotope
1017   evidence for the latitudinal distribution and wind speed dependence of the air-sea gas transfer velocity,
1018   Tellus, Serie B, 58B, 390-417, 2006.
1019   Large, W. G., and Yeager, S. G.: The global climatology of an interannually varying air–sea flux data set,
1020   Climate Dynamics, 33, 341-364, 10.1007/s00382-008-0441-3, 2009.
1021   Lawrence, C. R., Beem-Miller, J., Hoyt, A. M., Monroe, G., Sierra, C. A., Stoner, S., Heckman, K.,
1022   Blankinship, J. C., Crow, S. E., McNicol, G., Trumbore, S., Levine, P. A., Vindušková, O., Todd-Brown, K.,
1023   Rasmussen, C., Hicks Pries, C. E., Schädel, C., McFarlane, K., Doetterl, S., Hatté, C., He, Y., Treat, C.,
1024   Harden, J. W., Torn, M. S., Estop-Aragonés, C., Asefaw Berhe, A., Keiluweit, M., Della Rosa Kuhnen, Á.,
1025   Marin-Spiotta, E., Plante, A. F., Thompson, A., Shi, Z., Schimel, J. P., Vaughn, L. J. S., von Fromm, S. F., and
1026   Wagai, R.: An open-source database for the synthesis of soil radiocarbon data: International Soil

1027   Radiocarbon Database (ISRaD) version 1.0, Earth Syst. Sci. Data, 12, 61-76, 10.5194/essd-12-61-2020,
1028   2020.
1029   Lawrence, D. M., Fisher, R. A., Koven, C. D., Oleson, K. W., Swenson, S. C., Bonan, G., Collier, N., Ghimire,
1030   B., van Kampenhout, L., Kennedy, D., Kluzek, E., Lawrence, P. J., Li, F., Li, H., Lombardozzi, D., Riley, W. J.,
1031   Sacks, W. J., Shi, M., Vertenstein, M., Wieder, W. R., Xu, C., Ali, A. A., Badger, A. M., Bisht, G., van den
1032   Broeke, M., Brunke, M. A., Burns, S. P., Buzan, J., Clark, M., Craig, A., Dahlin, K., Drewniak, B., Fisher, J. B.,
1033   Flanner, M., Fox, A. M., Gentine, P., Hoffman, F., Keppel-Aleks, G., Knox, R., Kumar, S., Lenaerts, J., Leung,
1034   L. R., Lipscomb, W. H., Lu, Y., Pandey, A., Pelletier, J. D., Perket, J., Randerson, J. T., Ricciuto, D. M.,
1035   Sanderson, B. M., Slater, A., Subin, Z. M., Tang, J., Thomas, R. Q., Val Martin, M., and Zeng, X.: The
1036   Community Land Model Version 5: Description of New Features, Benchmarking, and Impact of Forcing
1037   Uncertainty, Journal of Advances in Modeling Earth Systems, 11, 4245-4287, 10.1029/2018MS001583,
1038   2019.
1039   Laws, E. A., Popp, B. N., Bidigare, R. R., Kennicutt, M. C., and Macko, S. A.: Dependence of phytoplankton
1040   carbon isotopic composition on growth rate and [CO2)aq: Theoretical considerations and experimental
1041   results, Geochimica et Cosmochimica Acta, 59, 1131-1138, https://doi.org/10.1016/0016-
1042   7037(95)00030-4, 1995.
1043   Levin, I., Naegler, T., Kromer, B., Diehl, M., Francey, R. J., Gomez-Pelaez, A. J., Steele, L. P., Wagenbach,
1044   D., Weller, R., and Worthy, D. E.: Observations and modelling of the global distribution and long-term
1045   trend of atmospheric 14CO2, Tellus B, 62, 26-46, 10.1111/j.1600-0889.2009.00446.x, 2010.
1046   Lombardozzi, D. L., Lu, Y., Lawrence, P. J., Lawrence, D. M., Swenson, S., Oleson, K. W., Wieder, W. R.,
1047   and Ainsworth, E. A.: Simulating Agriculture in the Community Land Model Version 5, Journal of
1048   Geophysical Research: Biogeosciences, 125, e2019JG005529, 10.1029/2019JG005529, 2020.
1049   Masarik, J., and Beer, J.: An updated simulation of particle fluxes and cosmogenic nuclide production in
1050   the Earth's atmosphere, Journal of Geophysical Research: Atmospheres, 114, D11103,
1051   10.1029/2008jd010557, 2009.
1052   Meinshausen, M., Vogel, E., Nauels, A., Lorbacher, K., Meinshausen, N., Etheridge, D. M., Fraser, P. J.,
1053   Montzka, S. A., Rayner, P. J., Trudinger, C. M., Krummel, P. B., Beyerle, U., Canadell, J. G., Daniel, J. S.,
1054   Enting, I. G., Law, R. M., Lunder, C. R., O'Doherty, S., Prinn, R. G., Reimann, S., Rubino, M., Velders, G. J.
1055   M., Vollmer, M. K., Wang, R. H. J., and Weiss, R.: Historical greenhouse gas concentrations for climate
1056   modelling (CMIP6), Geosci. Model Dev., 10, 2057-2116, 10.5194/gmd-10-2057-2017, 2017.
1057   Mook, W. G.: ^{13}C in atmospheric CO_2, Netherlands Journal of Sea Research, 20, 211-223, 1986.
1058   Moore, J. K., Doney, S. C., Kleypas, J. A., Glover, D. M., and Fung, I. Y.: An intermediate complexity marine
1059   ecosystem model for the global domain, Deep-Sea Research Part Ii-Topical Studies in Oceanography, 49,
1060   403-462, 2002.
1061   Moore, J. K., Doney, S. C., and Lindsay, K.: Upper ocean ecosystem dynamics and iron cycling in a global
1062   three-dimensional model, Global Biogeochemical Cycles, 18, 10.1029/2004GB002220, 2004.
1063   Mouchet, A.: The Ocean Bomb Radiocarbon Inventory Revisited, Radiocarbon, 55, 1580-1594,
1064   10.1017/S0033822200048505, 2013.
1065   Müller, S. A., Joos, F., Plattner, G. K., Edwards, N. R., and Stocker, T. F.: Modeled natural and excess
1066   radiocarbon: Sensitivities to the gas exchange formulation and ocean transport strength, Global
1067   Biogeochem. Cycles, 22, GB3011, doi:10.1029/2007GB003065, doi:10.1029/2007GB003065, 2008.
1068   Naegler, T., Ciais, P., Rodgers, K., and Levin, I.: Excess radiocarbon constraints on air-sea gas exchange
1069   and the uptake of CO2 by the oceans, Geophysical Research Letters, 33, 10.1029/2005GL025408, 2006.
1070   Naegler, T., and Levin, I.: Closing the global radiocarbon budget 1945–2005, Journal of Geophysical
1071   Research: Atmospheres, 111, n/a-n/a, 10.1029/2005jd006758, 2006.
1072   Naegler, T.: Reconciliation of excess 14C-constrained global CO2 piston velocity estimates, Tellus B, 61,
1073   372-384, 10.1111/j.1600-0889.2008.00408.x, 2009.
1074   Naegler, T., and Levin, I.: Observation-based global biospheric excess radiocarbon inventory 1963–2005,
1075   Journal of Geophysical Research: Atmospheres, 114, n/a-n/a, 10.1029/2008jd011100, 2009a.

1076   Naegler, T., and Levin, I.: Biosphere-atmosphere gross carbon exchange flux and the δ13CO2 and
1077   Δ14CO2 disequilibria constrained by the biospheric excess radiocarbon inventory, Journal of Geophysical
1078   Research: Atmospheres, 114, 10.1029/2008JD011116, 2009b.
1079   Oeschger, H., Siegenthaler, U., Schotterer, U., and Gugelmann, A.: A box diffusion model to study the
1080   carbon dioxide exchange in nature, Tellus, 27, 170-192, 1975.
1081   Oleson, K., Lawrence, D. M., Bonan, G. B., B. Drewniak, Huang, M., C.D. Koven, C. D., Levis, S., Li, F., Riley,
1082   W. J., Subin, Z. M., Swenson, S., Thornton, P. E., Bozbiyik, A., Fisher, R., C.L. Heald, C. L., Kluzek, E.,
1083   Lamarque, J. F., Lawrence, P. J., Leung, L. R., Lipscomb, W., Muszala, S. P., Ricciuto, D. M., Sacks, W. J.,
1084   Sun, Y., Tang, J., and Yang, Z.-L.: Technical description of version 4.5 of the Community Land Model
1085   (CLM), Boulder, CO, 420, 2013.
1086   Orr, J.C., Najjar, R. G., Sabine, C., and Joos, F.: OCMIP-2 Abiotic-HOWTO:
1087   http://www.ipsl.jussieu.fr/OCMIP/phase2/simulations/Abiotic/HOWTO-Abiotic.html, access: 18 July
1088   2012, 1999.
1089   Orr, J. C., Najjar, R. G., Aumont, O., Bopp, L., Bullister, J. L., Danabasoglu, G., Doney, S. C., Dunne, J. P.,
1090   Dutay, J. C., Graven, H., Griffies, S. M., John, J. G., Joos, F., Levin, I., Lindsay, K., Matear, R. J., McKinley, G.
1091   A., Mouchet, A., Oschlies, A., Romanou, A., Schlitzer, R., Tagliabue, A., Tanhua, T., and Yool, A.:
1092   Biogeochemical protocols and diagnostics for the CMIP6 Ocean Model Intercomparison Project (OMIP),
1093   Geosci. Model Dev., 10, 2169-2199, 10.5194/gmd-10-2169-2017, 2017.
1094   Peacock, S.: Debate over the ocean bomb radiocarbon sink: Closing the gap, Global Biogeochemical
1095   Cycles, 18, 10.1029/2003GB002211, 2004.
1096   Perez, F. F., Fontela, M., García-Ibáñez, M. I., Mercier, H., Velo, A., Lherminier, P., Zunino, P., de la Paz,
1097   M., Alonso-Pérez, F., Guallart, E. F., and Padin, X. A.: Meridional overturning circulation conveys fast
1098   acidification to the deep Atlantic Ocean, Nature, 554, 515, 10.1038/nature25493, 2018.
1099   Randerson, J. T., Enting, I. G., Schuur, E. A. G., Caldeira, K., and Fung, I. Y.: Seasonal and latitudinal
1100   variability of troposphere Δ14CO2: Post bomb contributions from fossil fuels, oceans, the stratosphere,
1101   and the terrestrial biosphere, Global Biogeochemical Cycles, 16, 59-51-59-19, 10.1029/2002GB001876,
1102   2002.
1103   Rath, H.: Simulation der globalen ^{85}Kr- und ^{14}CO$_2$-Verteilung mit Hilfe eines zeitabhängigen,
1104   zweidimensionalen Modells der Atmosphaäre, Ph.D., Univ. Heidelberg, Germany, Heidelberg, 1988.
1105   Reimer, P. e. a.: The IntCal20 Northern Hemisphere radiocarbon age calibration curve (0-55 kcal BP),
1106   Radiocarbon, accepted, 2020.
1107   Reimer, P. J., Austin, W. E. N., Bard, E., Bayliss, A., Blackwell, P. G., Bronk Ramsey, C., Butzin, M., Cheng,
1108   H., Edwards, R. L., Friedrich, M., Grootes, P. M., Guilderson, T. P., Hajdas, I., Heaton, T. J., Hogg, A. G.,
1109   Hughen, K. A., Kromer, B., Manning, S. W., Muscheler, R., Palmer, J. G., Pearson, C., van der Plicht, J.,
1110   Reimer, R. W., Richards, D. A., Scott, E. M., Southon, J. R., Turney, C. S. M., Wacker, L., Adolphi, F.,
1111   Büntgen, U., Capano, M., Fahrni, S. M., Fogtmann-Schulz, A., Friedrich, R., Köhler, P., Kudsk, S., Miyake,
1112   F., Olsen, J., Reinig, F., Sakamoto, M., Sookdeo, A., and Talamo, S.: The IntCal20 Northern Hemisphere
1113   Radiocarbon Age Calibration Curve (0–55 cal kBP), Radiocarbon, 62, 725-757, 10.1017/RDC.2020.41,
1114   2020.
1115   Revelle, R., and Suess, H. E.: Carbon dioxide exchange between atmosphere and ocean and the question
1116   of an increase of atmospheric CO$_2$ during the past decades, Tellus, 9, 18-27, 1957.
1117   Rodgers, K. B., Aumont, O., Madec, G., Menkes, C., Blanke, B., Monfray, P., Orr, J. C., and Schrag, D. P.:
1118   Radiocarbon as a thermocline proxy for the eastern equatorial Pacific, Geophysical Research Letters, 31,
1119   https://doi.org/10.1029/2004GL019764, 2004.
1120   Rodgers, K. B., Mikaloff-Fletcher, S. E., Bianchi, D., Beaulieu, C., Galbraith, E. D., Gnanadesikan, A., Hogg,
1121   A. G., Iudicone, D., Lintner, B. R., Naegler, T., Reimer, P. J., Sarmiento, J. L., and Slater, R. D.:
1122   Interhemispheric gradient of atmospheric radiocarbon reveals natural variability of Southern Ocean
1123   winds, Clim. Past, 7, 1123-1138, 10.5194/cp-7-1123-2011, 2011.

Roth, R., and Joos, F.: A reconstruction of radiocarbon production and total solar irradiance from the Holocene ^{14}C and CO_2 records: implications of data and model uncertainties, Clim. Past, 9, 1879-1909, 10.5194/cp-9-1879-2013, 2013.

Sabine, C. L., Feely, R. A., Gruber, N., Key, R. M., Lee, K., Bullister, J. L., Wanninkhof, R., Wong, C. S., Wallace, D. W. R., Tilbrook, B., Millero, F. J., Peng, T., Kozyr, A., Ono, T., and Rios, A. F.: The oceanic sink for anthropogenic CO_2, Science, 305, 367-371, 2004.

Schlitzer, R.: Assimilation of Radiocarbon and Chlorofluorocarbon Data to Constrain Deep and Bottom Water Transports in the World Ocean, Journal of Physical Oceanography, 37, 259-276, 10.1175/JPO3011.1, 2007.

Schmidt, A., Burr, G. S., Taylor, F. W., O'Malley, J., and Beck, J. W.: A semiannual radiocarbon record of a modern coral from the Solomon Islands, Nuclear Instruments and Methods in Physics Research Section B: Beam Interactions with Materials and Atoms, 223-224, 420-427, https://doi.org/10.1016/j.nimb.2004.04.080, 2004.

Shi, Z., Allison, S. D., He, Y., Levine, P. A., Hoyt, A. M., Beem-Miller, J., Zhu, Q., Wieder, W. R., Trumbore, S., and Randerson, J. T.: The age distribution of global soil carbon inferred from radiocarbon measurements, Nature Geoscience, 13, 555-559, 10.1038/s41561-020-0596-z, 2020.

Siegenthaler, U.: Carbon-14 in the oceans, in: Handbook of Environmental Isotope Geochemistry, edited by: Fritz, P., and Fontes, J. C., Elsevier, Amsterdam, 1989.

Siegenthaler, U., and Joos, F.: Use of a Simple-Model for Studying Oceanic Tracer Distributions and the Global Carbon-Cycle, Tellus Series B-Chemical and Physical Meteorology, 44, 186-207, 1992.

Stuiver, M., and Polach, H. A.: Discussion Reporting of 14C Data, Radiocarbon, 19, 355-363, 10.1017/S0033822200003672, 1977.

Suess, H. E.: Radiocarbon Concentration in Modern Wood, Science, 122, 415, 10.1126/science.122.3166.415-a, 1955.

Sweeney, C., Gloor, E., Jacobson, A. R., Key, R. M., McKinley, G., Sarmiento, J. L., and Wanninkhof, R.: Constraining global air-sea gas exchange for CO_2 with recent bomb ^{14}C measurements, Global Biogeochem. Cycles, 21, doi:10.1029/2006GB002784, 2007.

Talley, L. D.: Closure of the Global Overturning Circulation Through the Indian, Pacific, and Southern Oceans: Schematics and Transports, Oceanography, 26, 80–97, 2013.

Thompson, M. V., Randerson, J. T., Malmström, C. M., and Field, C. B.: Change in net primary production and heterotrophic respiration: How much is necessary to sustain the terrestrial carbon sink?, Global Biogeochemical Cycles, 10, 711-726, 10.1029/96gb01667, 1996.

Toggweiler, J. R., Dixon, K., and Bryan, K.: Simulations of radiocarbon in a coarse-resolution world ocean model: 1. Steady state prebomb distributions, Journal of Geophysical Research: Oceans, 94, 8217-8242, 10.1029/JC094iC06p08217, 1989.

Turnbull, J. C., Mikaloff Fletcher, S. E., Ansell, I., Brailsford, G. W., Moss, R. C., Norris, M. W., and Steinkamp, K.: Sixty years of radiocarbon dioxide measurements at Wellington, New Zealand: 1954–2014, Atmos. Chem. Phys., 17, 14771-14784, 10.5194/acp-17-14771-2017, 2017.

Wanninkhof, R.: Relationship between wind speed and gas exchange over the ocean, Journal of Geophysical Research: Oceans, 97, 7373-7382, https://doi.org/10.1029/92JC00188, 1992.

Wanninkhof, R.: Relationship between wind speed and gas exchange over the ocean revisited, Limnology and Oceanography: Methods, 12, 351-362, 10.4319/lom.2014.12.351, 2014.

Watson, A. J., Schuster, U., Shutler, J. D., Holding, T., Ashton, I. G. C., Landschützer, P., Woolf, D. K., and Goddijn-Murphy, L.: Revised estimates of ocean-atmosphere CO2 flux are consistent with ocean carbon inventory, Nature Communications, 11, 4422, 10.1038/s41467-020-18203-3, 2020.

Weiss, W., and Roether, W.: The rates of tritium input to the world oceans, Earth and Planetary Science Letters, 49, 435-446, https://doi.org/10.1016/0012-821X(80)90084-9, 1980.

Woolf, D. K., Shutler, J. D., Goddijn-Murphy, L., Watson, A. J., Chapron, B., Nightingale, P. D., Donlon, C. J., Piskozub, J., Yelland, M. J., Ashton, I., Holding, T., Schuster, U., Girard-Ardhuin, F., Grouazel, A., Piolle,

1173   J. F., Warren, M., Wrobel-Niedzwiecka, I., Land, P. E., Torres, R., Prytherch, J., Moat, B., Hanafin, J.,
1174   Ardhuin, F., and Paul, F.: Key Uncertainties in the Recent Air-Sea Flux of CO2, Global Biogeochemical
1175   Cycles, 33, 1548-1563, 10.1029/2018GB006041, 2019.
1176   Yang, X., North, R., and Romney, C.: CMR nuclear explosion database (revision 3), Cent. for Monit. Res.,
1177   U. S. Army Space and Missile Def. Command, Arlington, Va., Arlington, Va, 2000.
1178   Zazzeri, G., Acuña Yeomans, E., and Graven, H. D.: Global and Regional Emissions of Radiocarbon from
1179   Nuclear Power Plants from 1972 to 2016, Radiocarbon, 60, 1067-1081, 10.1017/RDC.2018.42, 2018.
1180   Zhang, J., Quay, P. D., and Wilbur, D. O.: Carbon isotope fractionation during gas-water exchange and
1181   dissolution of CO2, Geochimica et Cosmochimica Acta, 59, 107-114, https://doi.org/10.1016/0016-
1182   7037(95)91550-D, 1995.

1183